Nucleic Acids Research, 2025, **53**, gkaf180
https://doi.org/10.1093/nar/gkaf180
Methods

Optimizing gRNA selection for high-penetrance F0 CRISPR screening for interrogating disease gene function

Sheng-Jia Lin, Kevin Huang, Cassidy Petree, Wei Qin, Pratishtha Varshney, Gaurav K. Varshney*

Genes & Human Disease Research Program, Oklahoma Medical Research Foundation, Oklahoma City, OK 73104, United States

*To whom correspondence should be addressed. Tel: +1 405 271 2185; Email: gaurav-varshney@omrf.org

Abstract

Genes and genetic variants associated with human disease are continually being discovered, but validating their causative roles and mechanisms remains a significant challenge. CRISPR/Cas9 genome editing in model organisms like zebrafish can enable phenotypic characterization of founder generation (F0) knockouts (Crispants), but existing approaches are not amenable to high-throughput genetic screening due to high variability, cost, and low phenotype penetrance. To overcome these challenges, here we provide guide RNA (gRNA) selection rules that enable high phenotypic penetrance of up to three simultaneous knockouts in F0 animals following injection of 1–2 gRNAs per gene. We demonstrate a strong transcriptomic overlap in our F0 knockouts and stable knockout lines that take several months to generate. We systematically evaluated this approach across 324 gRNAs targeting 125 genes and demonstrated its utility in studying epistasis, characterizing paralogous genes, and validating human disease gene phenotypes across multiple tissues. Applying our approach in a high-throughput manner, we screened and identified 10 novel neurodevelopmental disorders and 50 hearing genes not previously studied in zebrafish. Altogether, our approach achieves high phenotypic penetrance using low numbers of gRNAs per gene in F0 zebrafish, offering a robust pipeline for rapidly characterizing candidate human disease genes.

Graphical abstract

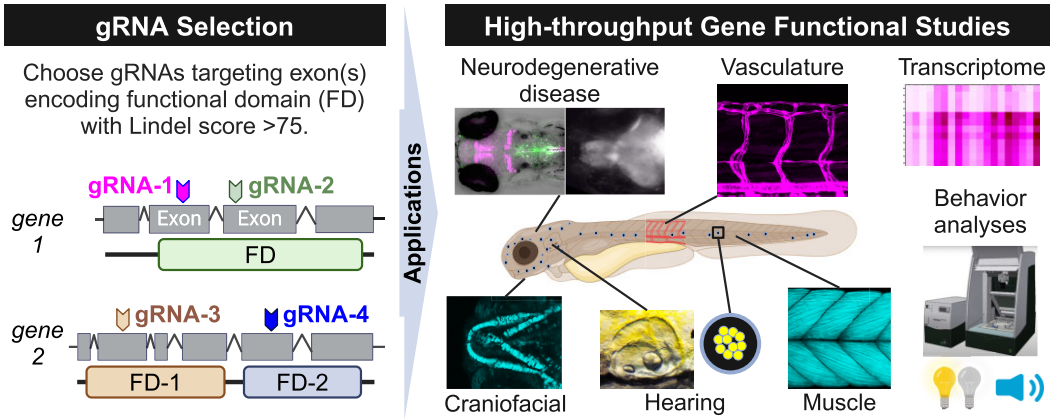

Introduction

The advent of low-cost whole genome sequencing has accelerated our understanding of human disease genetics [1], but a major challenge still remains to functionally validate and characterize candidate disease variants identified through correlative analyses like genome-wide association studies. The gold standard for functional validation is to disrupt the gene of interest or install precise disease gene variants into a model organism to assess a variant's phenotypic consequences and mechanism of action [2]. Among the available model organisms, zebrafish offer unique advantages, including rapid development and generation time, external fertilization, and optical transparency, which enable direct observation of phenotypes throughout the embryonic stages [3, 4].

Genome editing with CRISPR/Cas9 and related technologies has accelerated these functional studies in zebrafish [5–7], providing a means to generate knockout animals with precise genetic perturbations. Typically, this involves a time-consuming crossing scheme for about 6–9 months to generate the homozygous F2 generation—a process that is not

Received: June 7, 2024. **Revised:** February 14, 2025. **Editorial Decision:** February 17, 2025. **Accepted:** February 24, 2025

conducive to high-throughput screening of larger numbers of disease genes or variants. To overcome this limitation, several methods have been devised to analyze phenotypes in injected animals (founders, F0 generation), markedly reducing the time, labor, and cost associated with functional analysis [6, 8–12].

Phenotypic assessment in the F0 generation requires reliable biallelic gene disruption in founder animals, which poses challenges due to the poor correlation between predicted guide RNA (gRNA) efficiency, repair outcomes, and the resulting loss-of-function phenotype [13, 14]. To increase the chances of successfully disrupting gene function, previous methods employed a combination of three to four gRNAs to targeting the same coding sequence, achieving a disruption probability of up to 98% [9, 10, 12]. Adding complexity, one-third of zebrafish genome is duplicated, often necessitating the simultaneous disruption of two functionally redundant paralogs to observe a phenotype. However, using multiple gRNAs can result in 15–50% dysmorphic embryos [10], increased off-targets, and higher costs. While these F0 approaches are effective on a smaller scale, they are not suitable for high-throughput screening. Our work highlights that adoption of robust standardized methods utilizing fewer well-targeted gRNAs maintains high phenotype penetrance, low variability, and minimal mosaicism in order to enable efficient, large-scale validation of candidate human disease genes in zebrafish. Optimizing gRNA selection might help achieve this goal; however, most design tools are based on data from cell culture experiments, with the exception of CRISPRScan, which is developed using zebrafish and Xenopus data [15]. However, Uribe-Salazar *et al.* demonstrated poor concordance between predicted and observed gRNA editing efficiency [13]. Recently, a range of tools, such as Lindel, inDelphi, FORECasT, and RGEN, have been developed to predict the types and frequencies of insertions and deletions (indels) generated at a target site, focusing on predicted repair outcomes following double-strand breaks caused by Cas9 [16–20]. Naert *et al.* showed improved phenotype penetrance in both Xenopus and zebrafish using inDelphi scores; however, achieving over 90% of animals displaying a strong phenotype remains challenging [14].

By combining and adopting an optimal gRNA selection process, we show that we can significantly increase the penetrance of loss-of-function phenotypes when validating a large number of candidate human disease genes in zebrafish.

In this study, we thoroughly evaluated optimal gRNA selection strategies to develop a well-tested workflow capable of systematically providing low variability, high penetrance F0 zebrafish biallelic gene knockouts, which can enable high throughput phenotypic assessment of candidate human disease genes. We observed strong concordance between our F0 models and stable homozygous F2 zebrafish lines, both in phenotypic outcomes and transcriptomic responses to genetic perturbation.

As a proof-of-concept, we used this approach to functionally characterize 37 genes hypothesized to affect eight different organs/tissues in parallel. We also conducted a high-throughput screen of 63 genes implicated in hearing and vestibular function, demonstrating phenotypic defects for 52 genes. Altogether, this method provides a rigorously tested approach for scalable strategy for disease gene validation in zebrafish.

Materials and methods

Ethics statement and zebrafish husbandry

All animal care procedures were conducted in compliance with institutional and National Institutes of Health (NIH) guidelines and regulations. Zebrafish (*Danio rerio*) were housed and bred in a standard laboratory environment within an Association for Assessment and Accreditation of Laboratory Animal Care (AAALAC)-accredited facility at the Oklahoma Medical Research Foundation (OMRF). All experiments were performed in accordance with protocols 22–43, 22–67, and 22–76, approved by the OMRF Institutional Animal Care and Use Committee. Zebrafish work was carried out in the wild-type (WT) strain NHGRI-1 [21], *Tg(olig2:DsRed2;mnx1:EGFP)*, *Tg(kdrl:EGFP)* [22], *Tg(col2a1a:EGFP-CAAX)* [23], and *Tg(tuba1a:nls-Kal4FF;UAS:GCaMP7a);nacre* [24].

gRNA design, synthesis and microinjection for founder generation (F0) zebrafish

The coding sequences of 125 genes were obtained from the Ensembl Genome Browser, and their functional domains were annotated using either the Simple Modular Architecture Research Tool (SMART) [25, 26] or the DRSC Integrative Ortholog Prediction Tool (DIOPT) [27, 28] tools. DNA sequences encoding the functional domains were used to design 324 gRNAs across the 125 genes using the CRISPOR website [29]. CRISPOR incorporates predicted efficiency scores from algorithms such as Doench *et al.* [30], Chari *et al.* [31], Wang *et al.* [32], Moreno-Mateos (CRISPRScan [15]), and Stemmer (CCTop [33]), as well as predicted outcome scores from Bae *et al.* (RGEN [16]) and Chen *et al.* (Lindel [17]). Each gRNA sequence was further analyzed using CHOPCHOP (incorporated inDelphi [18, 19]) and FORECasT [20] tools to obtain additional predicted outcome scores. Target sequences starting with GG, NG, or GN were prioritized to ensure efficient transcription using the T7 promoter.

A total of 245 gRNAs were synthesized using *in vitro* transcription (IVT) as described earlier [7]. For *in vitro* synthesis, 20-nt sequences obtained from CRISPOR tool were appended with T7 promoter sequence (ttaatacgactcactata) at the 5′ end and partial crRNA/tracrRNA sequence (gttttagagctagaa) at the 3′ end. The resulting 53-nucleotide oligos, along with a 100-nucleotide crRNA/tracrRNA oligo were synthesized (IDT Technologies), annealed, and used as a template for gRNA synthesis using T7 HiScribe Kit (NEB, USA). The gRNAs were then purified using the Monarch RNA purification kit (NEB, USA). An additional 76 gRNAs were ordered as synthetic gRNAs with modifications at both ends including 74 single-gRNAs from Synthego, and two targets using Alt-R oligos from IDT. The complete list of gRNA target sequences can be found in Supplementary Table S1.

To generate F0 knockout embryos, a 6 μL mixture containing 1 μL of 40 μM Cas9-NLS protein (UC Berkeley QB3 Macrolab, Berkeley, CA), 2 μL of 1 M potassium chloride and 3 uL of gRNA(s) (1 μg for single gRNA injection or a maximum 3 μg for multiplex gRNAs injection) in nuclease-free water was injected into one-cell-stage WT embryos or appropriate transgenic reporter lines [8]. The crRNA:tracrRNA:Cas9 mixture was prepared following the method described in Hoshijima *et al.* [9] Injection volumes were calibrated to approximately 1.43 nL per injection (7.2 or 14.4 fmol of gRNA (s) and 9.33 fmol of Cas9 protein, approximately 1 or

1.5 gRNAs to 1 Cas9 protein). Injected embryos were raised at 28°C, and their development was monitored daily until 5 days post-fertilization (dpf).

Sanger sequencing, next-generation sequencing, and analyses for F0 knockouts

DNA was extracted from whole embryos (WT or F0) by dissolving them in 10 μL of 50 mM NaOH for 15 min at 95°C. Afterward, tissues were dissolved by properly by vortexing, and 15 μL of 100 mM Tris-HCl was added, followed by dilution at a 1:100. Polymerase chain reaction (PCR) amplification was carried out using a forward primer conjugated with M13 sequence (primer sequences are listed in Supplementary Table S1). The PCR products were purified using the DNA Clean & Concentrator-5 kit (ZYMO, USA) and subsequently sequenced using Sanger sequencing method. The sequencing results were analyzed using Tracking of Indels by DEcomposition (TIDE) [34], Synthego ICE (Inference of CRISPR Edits) tools and knockout scores were obtained from ICE tool.

For next-generation sequencing (NGS), genomic DNA was extracted from WT or F0 embryos using the same alkaline lysis method described above. After PCR fragment purification, the samples were subjected to paired-end read sequencing on the Illumina NGS platform (GENEWIZ, NJ, USA). The sequencing data were analyzed using CRISPResso2 [35].

Generation of stable knockouts and genotyping

Stable genetic knockouts for *cdh23*, *hars*, *gars1*, *coch*, *pou4f3*, *gipc3*, *tmprss3a/b*, *msrb3*, and *tbc1d24* were generated using the previously described CRISPR/Cas9 method [36, 37]. Founder fish injected with gRNA/Cas9 were raised and outcrossed with WT zebrafish (NHGRI-1). Adult F1 fish were fin-clipped for DNA extraction, and PCR products were analyzed by capillary electrophoresis as previously described [38]. Briefly, DNA was extracted from either adult fin clips or whole embryos by dissolving the tissue in 30 μL of 50 mM NaOH for 20 min at 95°C, adding 60 μL of 50 mM Tris-HCl, and diluted 1:100. PCR amplification was performed using a fluorescently labeled primer (FAM) (primer sequences were listed in Supplementary Table S1). Denatured PCR product sizes were measured on an Applied Biosystems 3500xL Genetic Analyzer using POP-7 polymer (Thermo Fisher Scientific, Cat # A26073). The results were analyzed by GeneMapper Software 6 (Thermo Fisher Scientific, Cat # A38888) as previously described comparing fragment sizes to WT product size. Heterozygous fish with two fragments indicating frameshifts mutations (not a multiple of 3) were selected. After ExoSAP-IT cleanup (Thermo Fisher Scientific), these PCR products were Sanger sequenced. Confirmed heterozygous carriers were incrossed for further analysis.

IVT of capped mRNA synthesis for rescue experiments

To rescue the observed phenotypes, we utilized the mRNA rescue method. We cloned cDNAs encoding zebrafish *wars1*, human *WARS1* and human *MED11* into the pCS2 + vector [39, 40]. Following *Not*I linearization, capped mRNAs were synthesized using the mMessage mMachine SP6 Transcription kit (Invitrogen, CA, USA). Synthesized mRNAs were then purified using the RNA clean & concentrator-5 kit (Zymo research, USA) and quantified using a nanodrop (DeNovix Inc, USA). For F0 knockout rescue, 150 picograms (pg) of either zebrafish *wars1* or human *WARS1* mRNA, or 200 pg of human *MED11* mRNA was co-injected with gRNAs/Cas9 protein into one-cell stage embryos.

Whole-mount *in situ* hybridization

To generate probes for whole-mount *in situ* hybridization (WISH), 500–700 base pairs cDNA fragments were synthesized using the SuperScript III One-step RT-PCR kit (Invitrogen, Cat # 12574–026) and gene-specific primers containing T3 and T7 tails in the forward and reverse primers, respectively (Supplementary Table S1). These amplicons were then used as templates for IVT of digoxigenin-UTP-labeled antisense riboprobes using DIG RNA labeling mix (Roche, Cat # 11277073910). The resulting RNA probes were purified with the RNA Clean & Concentrator-5 kit (Zymo, USA). WISH was performed as previously described [41].

Sample preparation for reverse transcription-quantitative PCR, RNA sequencing, and analysis

Total RNA was extracted from whole larvae using the TRIzol Reagent (Thermo Fisher Scientific, USA) and purified with the RNA Clean and Concentrator-5 kit (Zymo, USA), following the manufacturer's instructions. At 3 days post-fertilization (dpf), larvae were anesthetized with 168 mg/L Tricaine methanesulfonate (MS-222; Sigma-Aldrich, MO, USA) before extraction. Each experimental group consisted of three biological replicates, with six larvae randomly pooled per replicate. cDNA synthesis was performed using the iScript RT Supermix (Bio-Rad, CA, USA) and subsequently used as a template for reverse transcription-quantitative PCR (RT-qPCR) with SYBR Green Supermix (Thermo Fisher Scientific, CA, USA) on the LightCycler® 96 System (Roche, CA, USA). All RT-qPCR reactions were performed in biological triplicates with technical triplicates, using the 18S gene as a reference. Primer sequences for RT-qPCR are listed in Supplementary Table S1. Relative gene expression levels were calculated using the 2^(-ΔΔCt) method, with cycle threshold (Ct) values analyzed in Microsoft Excel. Total RNA was extracted from zebrafish embryos using TRIzol Reagent (Thermo Fisher Scientific, USA) and purified with the miRNeasy Mini kit (Qiagen, Hilden, Germany) following the manufacturer's protocols and earlier described method [42].

Differentially expressed genes (DEGs), comparisons, and visualization of bulk RNA-seq data were performed using the BxGenomics platform (BioInfoRx). DEGs were identified based on a P-value < 0.01 and a log2 fold change (log2FC) $\geq \pm 1$. This platform was also used to generate sample cluster dendrograms, sample-sample distances, heatmaps, volcano plots, Venn diagrams, gene expression plots, and Kyoto Encyclopedia of Genes and Genomes (KEGG) pathway analysis to interpret the results.

Hair cell development analysis

Hair cell quantification was performed on F0 knockout and control animals at 5 dpf. To visualize neuromast hair cells, embryos were stained with YO-PRO-1 Iodide (491/509) (Invitrogen, Cat # Y3603) as previously described [42]. Stained embryos were imaged in a lateral orientation, and hair cells within the posterior lateral line neuromasts (P1-P4) were quantified by counting stained nuclei using ImageJ.

Behavioral Phenotyping using LDTs, visual startle response, and acoustic evoked behavioral response

All behavior tests were performed at room temperature (RT), as previously described [43]. Briefly, to conduct the light-dark transition (LDT) test, larvae at 4 dpf were delicately moved into individual wells of a 96-well plate, each containing 150 μL of embryo water. The following day, the plate was placed into a Noldus chamber, and locomotion activity was recorded using the DanioVision system, which runs EthoVision XT software (Noldus Information Technology, Leesburg, VA, USA). Specifically, larvae at 5 dpf were allowed a 30-min habituation period in the light, followed by alternating 5-min periods of light and dark for three cycles. The locomotion activity of the larvae was measured in terms of distance traveled (in millimeters) per minute. The recorded values for each minute were then plotted using GraphPad Prism (GraphPad Software, San Diego, CA, USA). Larvae at 6 dpf were then subjected to VSR and acoustic evoked behavioral response (AEBR) tests, using either the Zebrabox (ViewPoint Life Sciences, Montreal, Canada) or the Noldus behavior chamber, as previously described [44, 45]. For VSR quantification, the number of responses to 5 stimuli for each larva was calculated as a percentage of the total responses. For AEBR quantification, the number of responses to 12 stimuli for each larva was calculated as a percentage of the total responses. Values were plotted using box and whisker plots generated by GraphPad Prism. Error bars indicate the range from the minimum to the maximum values, with the median value represented by the line in the center of the box.

Phalloidin staining assay

Larvae at 10 dpf were euthanized with tricaine and fixed in 4% (v/v) PFA at indicated developmental stages. The larvae were sequentially washed with 0.1% Triton X-100 in PBS (PBSTx, phosphate-buffered saline with Triton X-100) and incubated in Alexa Fluor 488 Phalloidin (1:100), (Invitrogen, Cat # A12379) in PBSTx at 4°C overnight. After a series of washes with PBSTx, the larvae were mounted laterally in 75% glycerol/PBS on glass slides.

Oil red O staining

Staining was performed as previously described by Kim *et al.* [46]. Briefly, 8 dpf larvae were fixed overnight in 4% PFA at 4°C. Following fixation, larvae were rinsed three times for 5 min each with 0.1% Tween-20 in PBS (PBSTw). Larvae were then stained for 15 min at RT in a solution of 300 μL 0.5% Oil Red O in 100% isopropyl alcohol and 200 μL of distilled water. After staining, larvae rinsed three times with PBSTw, followed by two 5-min rinses in 60% isopropyl alcohol. Larvae were briefly rinsed in PBSTw and then post-fixed in 4% PFA for 10 min. Finally, larvae were mounted in 75% glycerol for imaging.

Alcian blue staining

Cartilage development in the head of the 8 dpf larvae was visualized using a modified Alcian blue staining protocol [47]. Briefly, larvae were fixed overnight in 4% PFA at 4°C, then dehydrated through a graded ethanol series (20%, 50%, and 70% ethanol in distilled water) for 10 minutes each. Larvae were then incubated overnight at RT in 0.4% Alcian blue (8GX, Sigma-Aldrich, MO) in 70% ethanol with 80 mM $MgCl_2$ and incubated overnight at RT. After neutralization with saturated sodium tetraborate for at least 2 h, larvae were rinsed in distilled water, bleached for 20 min using 3% hydrogen peroxide and 1% potassium hydroxide (KOH), and rinsed again. Following two washes in PBSTw, tissue clearing was performed with 1% Trypsin for 1 hour at RT. Larvae were washed thrice with PBSTw, rinsed with 0.25% KOH, and passed through a graded glycerol series.

Pentylenetetrazole (PTZ) treatment

Larvae from *Tg(tuba1a:nls-Kal4FF;UAS:GCaMP7a);nacre* inbred ($n = 3$) at 5 dpf were individually mounted with 1.5% low melting point agarose (Sigma-Aldrich, USA) in a mm glass-bottom dish (Thermo Fisher Scientific). After solidification for 2 min, the larvae were filled with E3 medium and allowed to rest for 30 min. The medium was then replaced with either 15 mM PTZ (P6500, Sigma Aldrich, USA) or a PTZ-free E3 medium (used as negative controls). Imaging was conducted 20 minutes after the PTZ treatment.

Morphological phenotyping and imaging

For morphological phenotypes of F0 knockouts, animals at the proper developmental stage were randomly selected for imaging. Animals were manually oriented within 3% methylcellulose (Sigma, USA) under a stereomicroscope and photographed. The head length was measured by tracing a line from the tip of the snout to the end of the otic vesicle. Eye diameter was used for eye size measurements. All bright-field images were taken using either an Olympus SZX12 stereomicroscope equipped with an Olympus DP71 color digital camera (Olympus, Tokyo, Japan) or a high-definition Nikon DS-Fi2 camera mounted on a Nikon SMZ18 stereomicroscope (Nikon, Japan) for auto-Z-stacking pictures. For phenotyping from stable genetic knockouts, animals were randomly selected from heterozygous matings, and after imaging, animals were genotyped and matched back to the corresponding image. Images from transgenic zebrafish lines or phalloidin staining were acquired with a Zeiss LSM-710 confocal microscope.

Statistical analysis

The statistical analysis was conducted using GraphPad Prism. Data are presented as indicated in figure legends. For all analyses, the significance level was set at 0.05. Significance was determined using Brown-Forsythe and Welch's ANOVA with Dunnett's T3 multiple comparisons test for multiple comparisons, and two-tailed unpaired Student's *t*-test with Welch's correction for two comparisons, as detailed in the figure legends. *P*-values were represented as follows: not significant (ns) $P \geq 0.05$, $^{*}P < 0.05$, $^{**}P < 0.01$, $^{***}P < 0.001$, and $^{****}P < 0.0001$.

Results

Optimizing gRNA selection and target selection for high-efficiency F0 knockout

In this study, we aimed to evaluate an optimal and scalable knockout pipeline capable of introducing biallelic loss-of-function mutations in the F0 generation with high efficiency and strong phenotypic penetrance using just one or two gRNAs. First, we investigated the optimal gRNA concentration by titrating a gRNA (*slc45a2*) at various concentra-

tions (Supplementary Fig. S1A) and examining its correlation with phenotypic penetrance (pigmentation defects) and toxicity (dysmorphic phenotypes). The results revealed that a concentration of ~240 pg was sufficient to maximize gRNA efficiency. Higher concentration did not enhance phenotypic penetrance but increased the incidence of dysmorphic embryos (Supplementary Fig. S1B–D).

Next, we hypothesized that the key limitations of existing methods could be addressed by refining the gRNA selection process to identify high-efficiency gRNAs, thereby enhancing the penetrance of loss-of-function phenotypes. To explore this, we assessed how predicted gRNA efficiency (cleavage activity at the target site), predicted editing outcomes (likelihood of frameshift mutations or out-of-frame knockouts), and target site selection influenced phenotypic penetrance. For gRNA screening, we selected six characterized genes (*noto*, *rx3*, *slc45a2*, *rtf1*, *hars*, and *gars1)* with established homozygous lines that exhibit clear morphological abnormalities or pigmentation defects, facilitating phenotypic evaluation [48–51]. We used our previously established cloning-free method for gRNA synthesis to minimize cost [36].

For gRNA selection, we utilized the CRISPOR tool [29] to predict gRNA efficiencies and editing outcomes, as it included most of the algorithms such as CRISPRScan and Lindel scores. Additionally, we reanalyzed each gRNA sequence using CHOPCHOP (inDelphi score) and FORECasT to predict editing outcomes [18–20]. Prior studies suggested that targeting sequences encoding essential protein domains can increases the likelihood of disrupting gene function, even with in-frame mutations [52–54]. However, whether this principle applies universally or follows specific positional rules for loss-of-function phenotypes in vertebrate animal models has not been thoroughly validated [8].

To investigate, we designed gRNAs to target sites either inside (ID) or outside (OD) annotated functional protein domains of the target genes. We designed 51 gRNAs (35 ID and 16 OD) across the six target genes, with predicted efficiencies and outcome scores (ranging from 0 to 100, Supplementary Table S2). Each gRNA, or combinations of two gRNAs targeting the same gene, mixed with Cas9 protein to form an RNP complex, which was then injected into zebrafish embryos. Phenotypes of F0 knockouts were assessed at specific developmental stages and categorized as normal, intermediate, or strong compared to established homozygous knockout lines (Fig. 1A–D and Supplementary Fig. S2A and B). Dysmorphic phenotypes were also recorded (Supplementary Figs S1D and S2C). Phenotypic penetrance was graded on a scale of 0–5 based on the percentage of injected embryos exhibiting strong phenotypes (Fig. 1E).

Consistent with prior findings, ID-targeting gRNAs induced more robust phenotypes with higher penetrance than OD-targeting gRNAs, which showed variable phenotypic penetrance (Fig. 1F and Supplementary Table S2). Notably, gRNAs targeting the first half (*N*-terminal encoding sequences) of the functional domain significantly increased phenotypic penetrance compared to those targeting the latter half (*C*-terminal encoding sequences). The gRNAs targeting the C-terminal of the functional domain showed variable phenotypic penetrance, as evidenced in multiple cases: *noto_9*, *rx3_9*, *rtf1_5–8*, *hars_3–6*, and *gars1_3* (Fig. 1A-D, Supplementary Fig. S2A,B, and Supplementary Table S2). Similarly, variable results were observed with gRNAs targeting regions too close to the end of the coding sequence (CDS), such as *slc45a2_13* and _14. We also noted that lower phenotypic penetrance correlated with predicted gRNA scores falling below mean values across different prediction tools, as demonstrated by *rx3_6* and *rtf1_4* (Supplementary Table S2).

And using two gRNAs (either both ID or at least one ID) produced strong phenotypes with penetrance up to 100% while dysmorphic phenotypes generally less than 5% (Fig. 1A–C, Supplementary Fig. S1A and B and Supplementary Table S2). Low phenotypic penetrance also occurred in cases when the two gRNA target sites are very close together (e.g. Fig. 1B: *rx3_1 + 2* (14 bp distance between cutting sites), 1 + 3 (47 bp distance), and 2 + 3 (61 bp distance); Fig. 1C: *slc45a2_1 + 2* (21 bp distance), 1 + 3 (96 bp distance), and 2 + 3 (75 bp distance)). Examining gRNAs that achieved the highest phenotypic penetrance (Grade 5, where > 80% of injected animals showed a strong phenotype), we found that predicted efficiency from Stemmer (CCTop) scores and the predicted outcome from Lindel scores were generally higher and had relatively lower standard deviation compared to other tools (Fig. 1G).

Additionally, we raised the F0 knockouts to adulthood and found that the phenotypes observed in early embryos are consistent in the adult stage for these non-lethal genes. For example, aberrant pigmentation phenotypes remain until adulthood and are identical to what is observed in the stable homozygous knockout lines (Supplementary Fig. S3A and B).

Together, selecting gRNAs targeting the first (*N*-terminal) half of the functional domain and having high prediction scores is key to achieving a strong loss-of-function phenotype with high penetrance when using the F0 method.

Strong phenotypic penetrance correlates positively with editing outcome prediction tools

To further investigate the relationships between predicted efficiency, editing outcomes, and experimental results, we performed Sanger sequencing for 41 gRNA-targeted loci and analyzed data using TIDE, Synthego's ICE tools. Higher Lindel scores (>75) corresponded to high KO scores, while lower Lindel scores (<75) corresponded to low KO scores (Fig. 2A and B; Supplementary Table S2). However, no significant correlation was observed with Lindel score and editing efficiency. This observation was further confirmed by NGS deep sequencing results (Supplementary Figs S4–S7).

Pearson correlation heatmap analysis revealed that the prediction tools exhibited varying degrees of positive correlation depending on their specific functions (Fig. 2C). Notably, inDelphi, Lindel, and FORECasT showed strong positive correlations (Pearson $r > 0.5$) with each other and with observed KO scores. We also included data on strong phenotype penetrance (percentage of animals exhibiting a strong phenotype; $n = 51$ gRNAs) and RT-qPCR analysis (log2 fold change; $n = 41$ gRNAs) for each target (Fig. 2C; Supplementary Table S2). RT-qPCR results exhibited a weak-to-moderate negative correlation with editing outcome prediction tools (Lindel > inDelphi > FORECasT = RGEN) and observed KO scores. These findings suggest that editing outcome prediction tools can be relied for predicting frameshift mutations that lead to premature termination codons (PTCs), which in turn trigger nonsense-mediated decay (NMD) of the mutated mRNA. Analysis of data from the first half of the functional domains revealed strong positive correlations between editing outcome

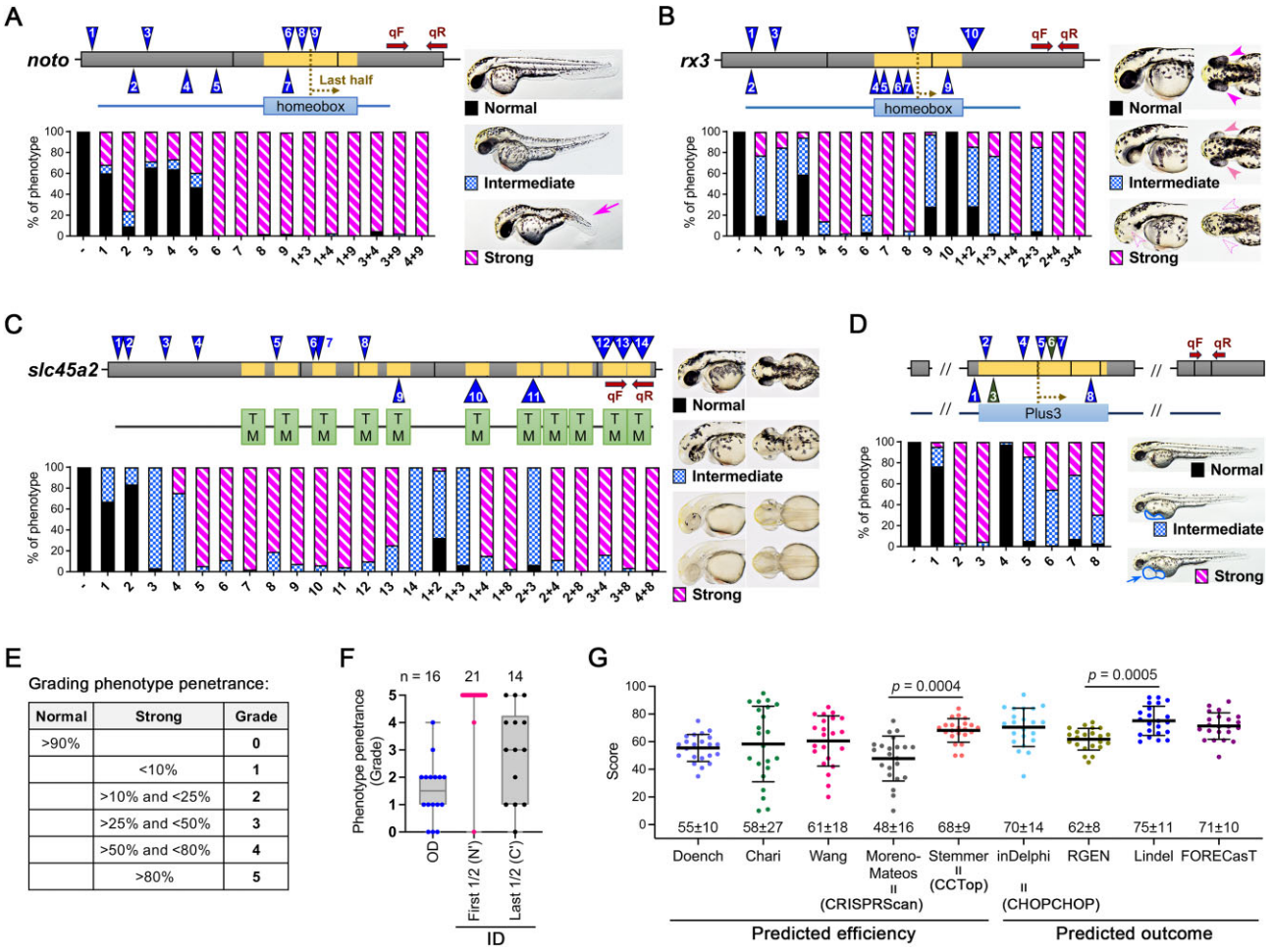

Figure 1. Examination of the relationship between predicted scores from online tools and phenotype penetrance for each gRNA. Four genes were selected based on the knockout phenotype, which includes (**A**) absence of notochord (arrow) in *noto* knockout at 2 dpf, (**B**) missing eyes (arrowheads) in *rx3* knockout at 2 dpf, (**C**) lack of pigmentation in *slc45a2* knockout at 3 dpf, and (**D**) pericardial edema (arrow and closed circle) in *rtf1* knockout at 2 dpf. The gRNAs (indicated by numbered triangles) were designed across gene exons (gray boxes) and the corresponding functional domain (s) encoded by exons (yellow boxes) for each gene were displayed in colored boxes below. Brown arrows indicate the forward (qF) and reverse (qR) primer for RT-qPCR. The introns were removed to simplify the schematics. The injected animals were first categorized by morphological phenotype as shown in each figure in the right panel and then calculated as a percentage of the total. The editing efficiency of each gRNA was analyzed using TIDE and ICE. (**E**) Grade 0 indicates that over 90% of injected animals for a gRNA exhibit no effect on phenotype; Grade 1 indicates that less than 10% fall into the strong category; Grade 2 indicates that between 10% and less than 25% are in the strong category; Grade 3 indicates that between 25% and less than 50% belong to the strong category; Grade 4 indicates that between 50% and less than 80% are categorized in the strong category; Grade 5 indicates that over 80% are classified in the strong category. (**F**) Quantification of phenotype penetrance for gRNAs targeting outside (OD) and inside (ID) of the functional domain. Each dot represents one gRNA. (**G**) A scatter plot was used to visualize the distribution of predicted scores for a gRNA generated from different online tools. Each dot represents one gRNA, and the mean value ± standard deviation (SD) of each group is placed at the bottom of the respective bar in the figure..

prediction tools and observed results, including TIDE, ICE, KO scores, and strong phenotype penetrance. Additionally, there were strong negative correlations with RT-qPCR results (Fig. 2D). These findings suggest that editing outcome prediction tools are reliable for selecting gRNAs that maximize editing efficiency, highest phenotype penetrance, and NMD induction.

In summary, our data indicate that high phenotypic penetrance in F0 zebrafish is better achieved by selecting gRNAs targeting the sequences encoding the N-terminus of a functional domain, i.e. the first half of the functional domain, which is termed the "first-half domain rule." Additionally, selecting gRNAs with Lindel scores above 75 enhances the likelihood of success of achieving high phenotypic penetrance. Although the FORECasT tool slightly outperformed Lindel, we recommend prioritizing Lindel scores using the CRISPOR tool, as it integrates multiple prediction tools, including off-target predictions, for systematic gRNA selection. Alternatively, one can verify gRNA scores using the FORECasT tool to ensure they exceed 70.

Comparison of the optimized approach with existing F0 knockout approaches

Currently, the most commonly used methods for F0 mutagenesis include the use of four random *in vitro* transcribed gRNAs, multiple synthetic gRNAs, or dual-gRNAs (dgRNAs combine chemically synthesized crRNA and tracrRNA into a crRNA:tracrRNA). To compare our optimized approach with existing methods, we synthesized four gRNAs from Wu *et al.*

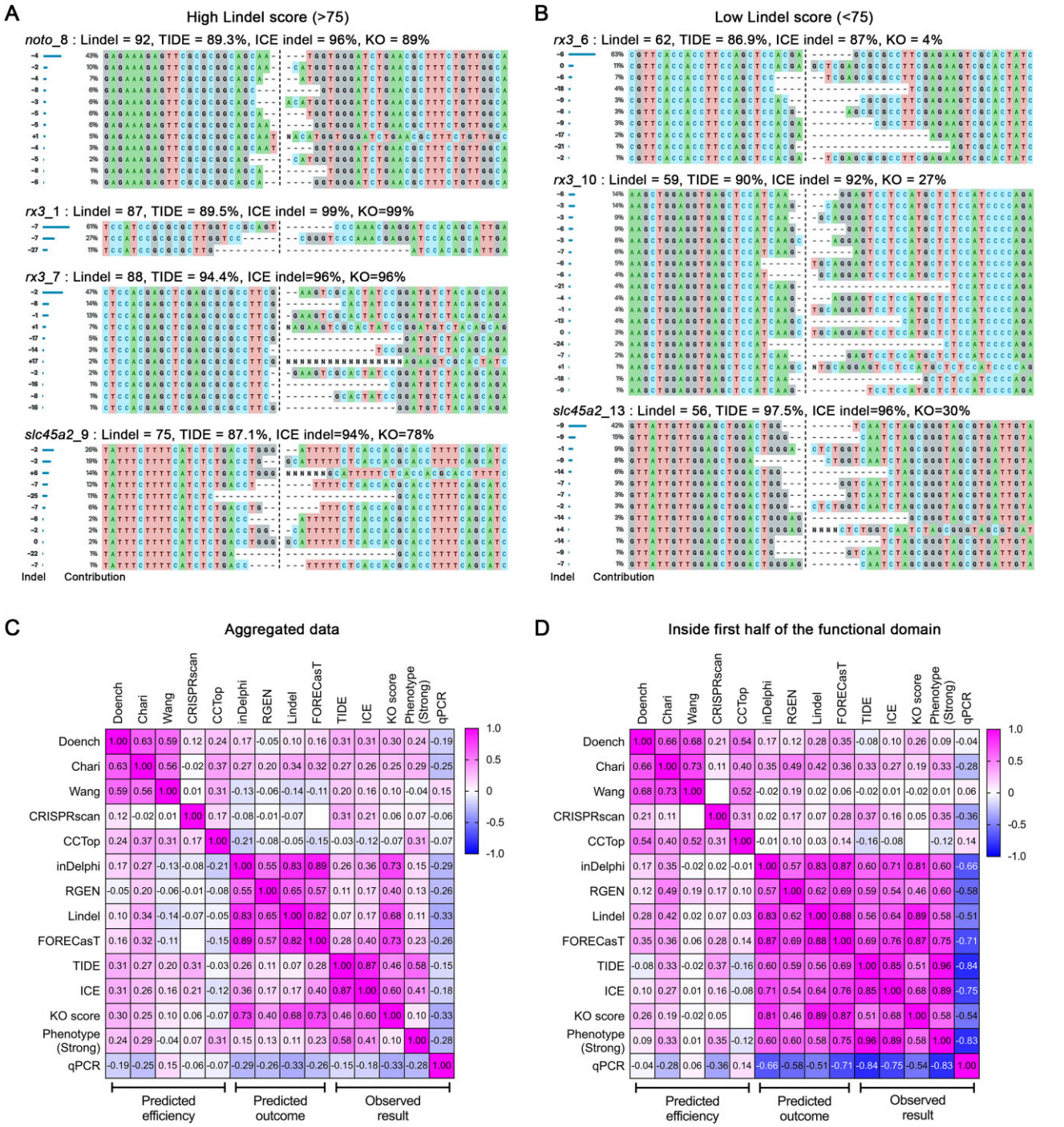

Figure 2. Predicted versus observed knockout efficiency correlations and Indel distributions across gRNAs. Synthego ICE analysis showing indel distributions for each gRNA scoring >75 in Lindel shown in (**A**) and those scoring <75 shown in (**B**). Panels (**C**) and (**D**) present heatmap visualizations of Pearson correlations between observed results and various prediction tools, including editing efficiency (TIDE and ICE), knockout (KO) score, strong phenotype penetrance, and RT-qPCR. Panel (**C**) summarizes aggregated data, while panel (**D**) focuses on gRNAs targeting the first half of the functional domain. Positive correlations (Pearson coefficient $r > 0$) are shown in magenta, while negative correlations ($r < 0$) are displayed in blue.

[12], and one or two gRNAs targeting *tbx16*, *slc24a5*, and *tbx5a* using our approach were synthesized via IVT (Fig. 3A–C). Additionally, we examined the phenotype penetrance using synthetic gRNA, and IVT gRNAs, as the 5′-GG requirement for efficient IVT by T7 RNA polymerase, (or GA for SP6) may limit the availability of effective guides within a given target region [5, 7].

As expected, using four random IVT gRNAs targeting exons resulted in strong phenotype penetrance but also caused a higher proportion of dysmorphic embryos (Fig. 3A and B and Supplementary Fig. S2D). In contrast, gRNAs selected using our optimized approach consistently exhibited strong phenotype penetrance, either comparable to (Fig. 3A and C) or exceeding (Fig. 3B) that of the four gRNAs, while significantly reducing dysmorphic phenotypes. Furthermore, synthetic gR-

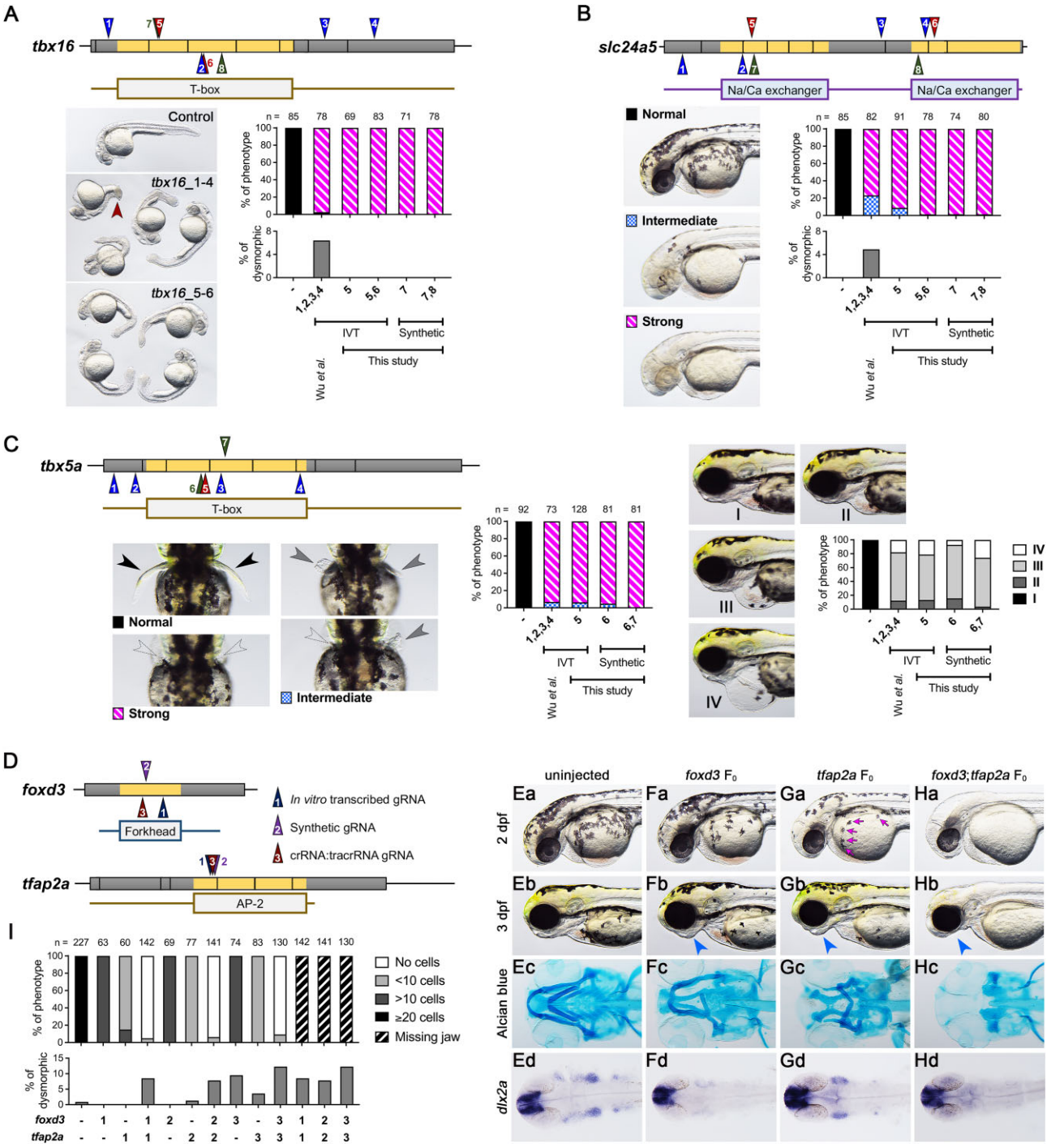

Figure 3. Comparison of phenotype penetrance across current F0 knockout methods. gRNAs targeting *tbx16* (**A**), *slc24a5* (**B**), and *tbx5a* (**C**) were obtained either from the methods described by Wu *et al.* (gRNAs 1–4; blue triangles) or our selection approach (gRNAs 5–8 for *tbx16* and *slc24a5*, and gRNAs 5–7 for *tbx5a*; brown triangles). These gRNAs were synthesized via IVT or chemical synthesis (green triangles). (**A**) *Tbx16* F0 embryos exhibited a curved tail phenotype at 1 dpf. The brown arrowhead highlights a kinked tail phenotype, which is distinct from the commonly observed curved tail phenotype in *tbx16* knockouts. (**B**) At 2 dpf, *slc24a5* F0 embryos displayed a lack of pigment cells, although some F0 embryos exhibited dysmorphic phenotypes (Supplementary Fig. S2D). (**C**) *Tbx5a* F0 embryos showed both pectoral fin loss and heart edema at 3 dpf. Black arrowheads indicate normal pectoral fins, gray arrowheads indicate shorter or kinked fins, and empty arrowheads denote the absence of pectoral fins. Representative images of heart edema graded I to IV, and corresponding quantifications post-injection are presented in the right panel. (**D**) Cartoon diagrams illustrate gRNA positions: synthesized via IVT (gRNA_1), chemically synthesized (gRNA_2), or chemically synthesized and assembled into crRNA:tracrRNA complexes (gRNA_3) for *foxd3* and *tfap2a* genes. (**E**–**H**) Representative phenotypes for uninjected, *foxd3* F0, *tfap2a* F0, and *foxd3;tfap2a* F0 embryos include pigmentation phenotypes at 2 dpf (Ea-Ha), aberrant lower jaw morphology at 3 dpf (Eb-Hb), abnormal Alcian blue cartilage staining at 5 dpf (Ec-Hc), and expression patterns of the pharyngeal arch progenitor marker *dlx2a* (Ed-Hd). Magenta arrows indicate pigment cells, while blue arrows denote aberrant lower jaws. (**I**) Phenotype quantifications were performed for the number of pigment cells on the yolk sac in 2 dpf embryos and for embryos with missing lower jaws at 3 dpf. Additional dysmorphic phenotypes are shown in Supplementary Fig. S2E.

NAs selected with our method showed an equal or improved phenotype penetrance compared to IVT gRNAs (Fig. 3A–C).

Next, we compared our approach to a study that used dgRNAs targeting both *foxd3* and *tfap2a* to achieve strong phenotype penetrance, such as loss pigmentation and missing jaw in double knockouts [9]. Three gRNAs were designed to target *foxd3* - one IVT gRNA (Lindel: 80; number 1), one synthetic gRNA (Lindel score: 90; number 2), and one dgRNA (Lindel score: 67; number 3) from Hoshijima *et al.* (Fig. 3D). Similarly, three gRNAs were designed to target *tfap2a* - one IVT gRNA (Lindel score: 84), one synthetic gRNA (Lindel score: 86), and one dgRNA (Lindel score: 85). Due to challenges in identifying a good IVT gRNA targeting the first half of the forkhead domain of *foxd3*, we selected an sgRNA (*foxd3*_1) targeting the later part of the domain. (Fig. 3D).

As previously reported in studies on F0s [9] and stable knockouts [55], *foxd3* F0s showed a mild reduction in pigment cells (10–20 cells) on the yolk sac (Fig. 3Fa), a dysmorphic jaw phenotype (Fig. 3Fb and Fc) and a significant reduction in the expression of the pharyngeal arch progenitor marker *dlx2a* (Fig. 3Fd). In contrast, *tfap2a* F0s exhibited a more severe reduction in pigment cells (fewer than 10) on the yolk sac (Fig. 3Ga), a dysmorphic jaw phenotype (Fig. 3Gb and Gc) and a partial decrease in *dlx2a* expression (Fig. 3Gd). Double F0 knockout of *foxd3* and *tfap2a* resulted in a complete loss of pigment cells on the yolk sac (Fig. 3Ha), a missing jaw (Fig. 3Hb and Hc), and a complete loss of *dlx2a* expression (Fig. 3Hd). Quantification of pigment cell counts across genotypes and gRNA types revealed that IVT gRNA, synthetic gRNA, and dgRNA produced a similar degree of strong phenotype penetrance in F0 knockouts (Fig. 3I). However, a higher proportion of dysmorphic embryos was observed in dgRNA-injected group (Fig. 3I and Supplementary Fig. S2E), potentially due to the high number of predicted off-target sites (152 off-targets) identified using CRISPOR.

In summary, our comparative analysis demonstrated that carefully selected gRNAs–either one or two–are sufficient to achieve consistent and high phenotype penetrance with low toxicity, outperforming the use of four random gRNAs.

Optimized multiplex F0 mutagenesis for studying epistasis, duplicated genes, and genetic pathways.

Polygenic disorders, characterized by the interplay of multiple genes, are significantly more common in humans than monogenic disorders caused by single gene mutations [56]. Zebrafish could provide a fast and robust model system in which to dissect gene interactions implicated in human polygenic disease, but only with the development of reliable approaches for simultaneously disrupting multiple genes in the F0 generation. Further emphasizing this need is the fact that one third of the zebrafish genome is duplicated, and this redundancy combined with reports of genetic compensation [57–59] necessitate the ability to efficiently target multiple genes [4]. While previous reports have demonstrated the ability to target up to three genes simultaneously, these approaches required between 9 and 12 gRNAs and typically resulted in high toxicity and/or unacceptable levels of off-target gene disruption in injected animals [10, 12].

As the experiments above demonstrate that our gRNA selection approach can achieve efficient double knockouts, we further aimed to establish a proof-of-concept for multiplex biallelic mutations in the F0 generation. We targeted three genes with known morphological phenotypes (*noto*_8, *rx3*_5, and *slc45a2*_9) simultaneously, using one gRNA for each, resulting in 95% (40/42) embryos exhibiting all three phenotypes (Supplementary Fig. S8). Therefore, we demonstrate the ability to achieve high phenotypic penetrance using just one well-designed gRNA per gene for a triple knockout.

Next, we tested this approach by knocking out multiple genes in a genetic pathway, focusing here on the highly redundant fibroblast growth factor receptors (FGFRs). Double and triple knockouts of *fgfr1a*, *fgfr1b*, and *fgfr2* exhibit morphological defects, including a kinked tail, loss of pectoral fins, and aberrant otic vesicle development, with varying severity [60]. All guides showed editing efficiencies in the range of 70–90%. Using the criteria and score thresholds established above, we designed three gRNAs for each gene: two targeting near the beginning of the CDS (OD gRNAs) and one targeting the sequence encoding the kinase domain (ID gRNA) (Fig. 4A). As expected, only the ID gRNAs induced pronounced phenotypes (Fig. 4B–D), regardless of editing efficiency or co-injection of two OD gRNAs.

Consistent with previous findings in stable knockouts, the *fgfr1a;fgfr2* double knockout resulted in moderate phenotypes such as a kinked tail (Fig. 4B) and defective pectoral fins (Fig. 4C). The *fgfr1a;fgfr1b* double knockouts showed even more severe tail and fin defects, along with additional abnormal otoliths (Fig. 4D). Animals with triple knockouts exhibited even more severe otolith abnormalities with higher penetrance, increasing from 45% in the double F0 to 88% in the triple F0.

Both double and triple F0 knockouts recapitulated previous findings in double and triple stable homozygous knockouts [60], validating our approach and highlighting the value of assessing multiple gene knockouts in the F0 generation.

To apply multiplexed gene knockout as a proof-of-concept to study epistasis, we next aimed to simultaneously knock out the tumor suppressor LLGL scribble cell polarity complex component 2 (*llgl2*) and the oncogene erb-b2 receptor tyrosine kinase 2 (*erbb2*). Previous studies have shown that disruption of *erbb2* is sufficient to alleviate the epithelial-mesenchymal transition (EMT) phenotype of *llgl2* knockouts [61, 62]. We designed three ID gRNAs for each gene (Fig. 4E), and editing efficiency for each gRNA was confirmed (Fig. 4F).

We found that injecting two ID gRNAs targeting *llgl2* induced EMT in 84–92% of F0 knockouts, while two ID gRNAs targeting *erbb2* resulted in the established aberrant fin fold phenotype in 86–91% of F0 knockouts (Fig. 4G–I and K). Given that the LLGL domain of Llgl2 and the kinase domain of Erbb2 are key functional regions, and that two ID gRNAs produced strong phenotype penetrance, we co-injected four gRNAs targeting *llgl2* and *erbb2* (target numbers 2 and 3 for each gene), which rescued the neoplastic phenotype in 64% of F0 knockouts (Fig. 4J, J', and K). Additionally, we did not observe any dysmorphic phenotypes other than the expected knockout phenotypes.

Our findings suggest that using one or two gRNAs per gene enables the knockout of at least three genes without causing noticeable toxicity in zebrafish. This is significant because other commonly used methods typically require 3–4 guides, making it more challenging to simultaneously knock out 2–3 genes.

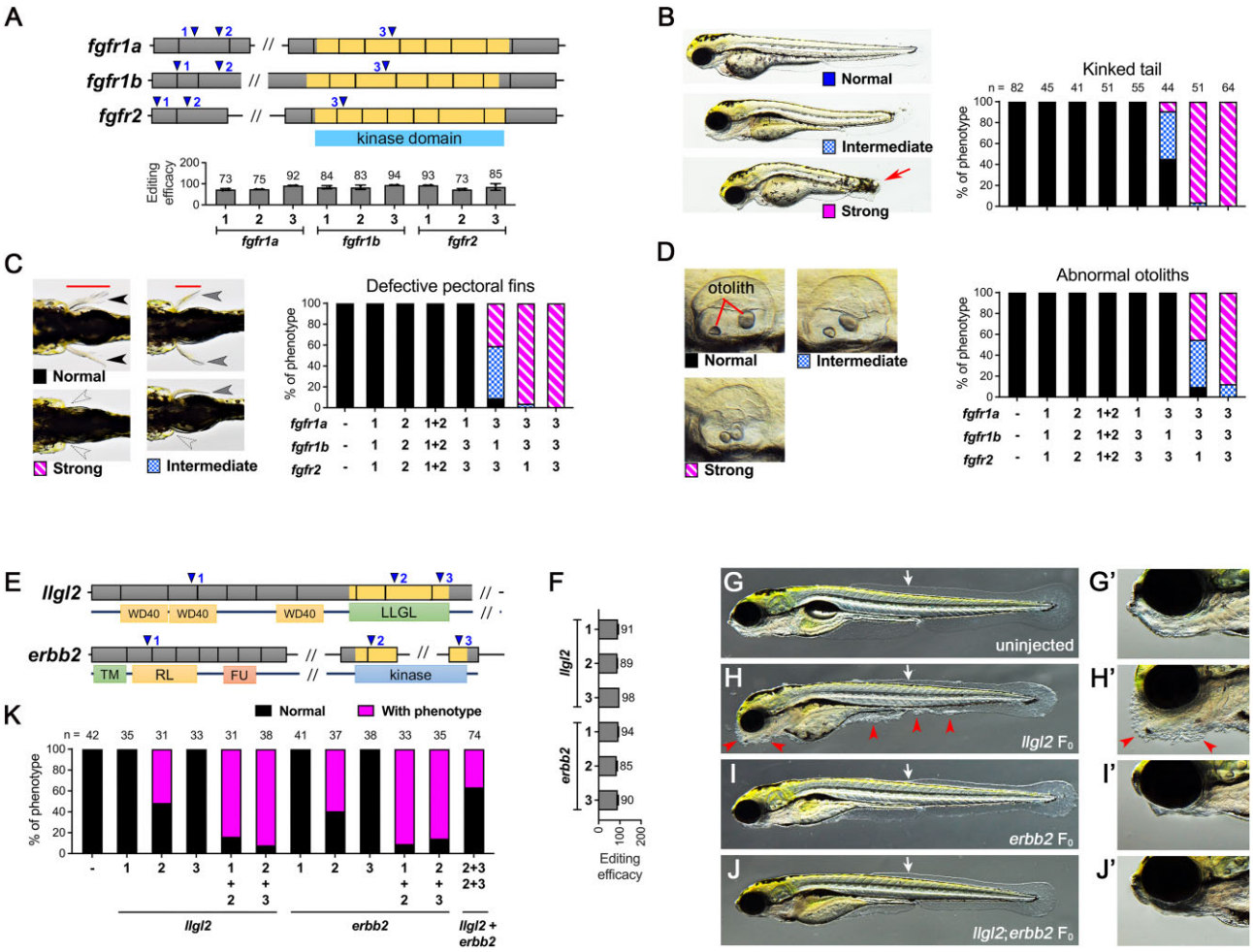

Figure 4. Multiplex mutagenesis for duplicated genes and synthetic rescue using F0 approach. (**A**) Schematics of gRNA target loci (blue triangle), gene exons (gray boxes) and their corresponding kinase domain (yellow boxes) for *fgfr1a*, *fgfr1b* and *fgfr2* are shown. gRNA_1 and gRNA_2 target the beginning of the gene, while gRNA_3 targets the exon encoding the kinase domain. Editing efficiency for each gRNA was shown below. Representative phenotypic images for (**B**) kinked tail, (**C**) defective pectoral fins, and (**D**) abnormal otoliths of F0 animals at 3 dpf, along with their quantification results for different gRNA combinations, are presented. For phenotype categorization, animals showing either a kinked tail (indicated by red arrow in B), complete absence of both fins (**C**), or two otoliths stuck together (**D**) are considered in the strong category. (**E**) Schematics of gRNA target loci, exons, and corresponding functional domains for both *Ilgl2* and *erbb2* are depicted. The exons encoding LLGL domain for *Ilgl2* and the kinase domain for *erbb2* are shown in yellow boxes. (**F**) Editing efficiency for each gRNA. (**G**–**J**) Representative images for uninjected, *Ilgl2* F0, *erbb2* F0 and *Ilgl2;erbb2* F0 at 5 dpf. The white arrow indicates the beginning position of the dorsal fin fold observed in *erbb2* F0 knockouts, and red arrowheads indicated the uncontrolled proliferation of epidermal cells. The lower jaw image was enlarged in (G'-J'). Because these phenotypes are difficult to quantify the severity, animals showing excessive epidermal cells were counted with phenotype for *Ilgl2* F0 knockouts, and animals showing aberrant dorsal fin fold and missing lower jaw were counted as phenotype for *erbb2* F0 knockouts. For the *Ilgl2;erbb2* F0 group, animals showing either excessive epidermal cells or aberrant dorsal fin fold or missing lower jaw were counted as phenotype. We didn't see any dysmorphic (phenotypes other than characterized) animals in these experiments. (**K**) Quantifications of animals with phenotypes as shown in (G-J).

Gene expression profiles validate F0 CRISPR knockouts as reliable alternatives to stable zebrafish lines

Given the high phenotypic resemblance between F0 and stable knockouts, we investigated whether their gene expression profiles exhibited similar patterns. First, contrary to a previous study that suggested microinjection can trigger a wound-healing response in injected animals [13], we demonstrated that Cas9 injection in F0 zebrafish does not induce major or consistently observed gene expression changes compared to uninjected embryos as assessed by RNA-seq (Fig. 5A and Supplementary Fig. S9A).

Next, we performed RNA-seq to compare gene expression profiles of WT, F0 stable homozygous knockout, and mRNA-rescued F0 animals, making the first transcriptomic analysis of rescued animals. Utilizing our prior study on tryptophanyl-tRNA synthetase 1 (*wars1*), we employed four gRNAs targeting the kinase domain [39, 63]. Editing efficiencies were validated through Sanger sequencing (Fig. 5B). A stable knockout generated in the earlier study using the *wars1*_2 gRNA showed a two-base-pair deletion, designated as *wars1*-/-, confirmed via Sanger sequencing (Fig. 5C). The microcephaly phenotype observed in both *wars1*-/- and *wars1* F0 knockouts was successfully rescued by co-injection of zebrafish or human mRNA encoding *wars1*/*WARS1* (Fig. 5C).

Clustering of RNA-seq profiles revealed two distinct groups based on genetic lineage. Group 1 encompassed all F0 knockouts, further subdivided into uninjected, Cas9 injected, and rescued F0 animals. Group 2 included stable homozygous knockouts (-/-), clustered separately from their WT siblings

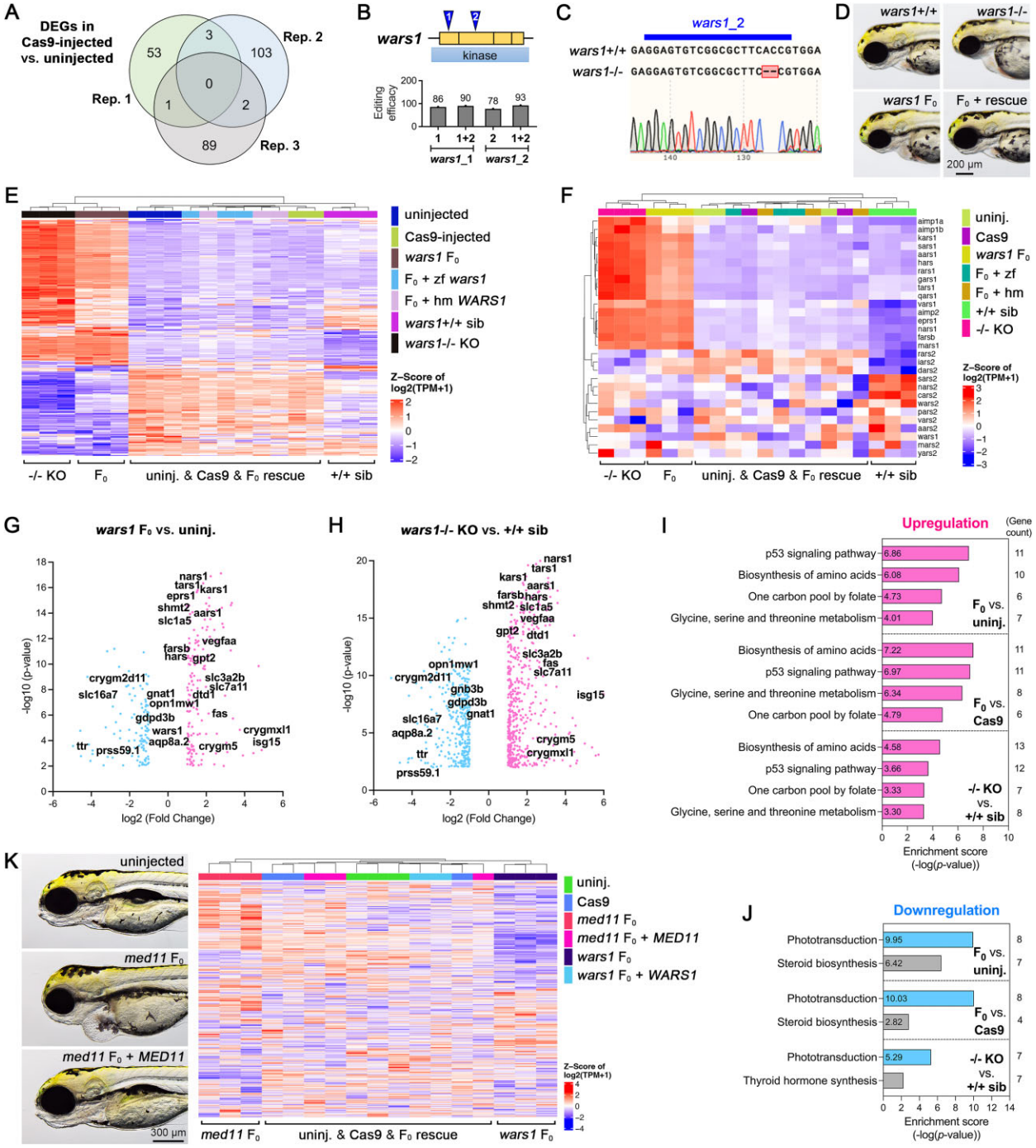

Figure 5. Comprehensive transcriptomic analysis of uninjected and Cas9-injected control, F0, stable knockout, and rescued animals. (**A**) A Venn diagram compares DEGs in Cas9-injected versus uninjected embryos at 3 dpf. Three replicates indicate three independent runs of RNA-sequencing (RNA-seq), with each replicate containing biological triplicates ($n = 6$ embryos for each biological replicate). (**B**) Schematics of two gRNA target loci (blue triangle) and exons encoding kinase domain (yellow boxes) for the *wars1* gene. The editing efficiency for each gRNA, injected either individually or in combination, is shown below. (**C**) Sequence alignment and chromatogram showing a 4bp deletion in the *wars1* stable mutant generated by the *wars1_2* gRNA, as revealed by Sanger sequencing. (**D**) Representative images of morphology for *wars1* WT sibling (*wars1*+/+), homozygous knockout (*wars1*-/-), F0 and F0 rescued with human *WARS1* mRNA embryos at 3dpf. Lateral view and anterior to the left. (**E**) A heatmap visualization of DEGs in uninjected (uninj.), Cas9 protein-injected (Cas9), *wars1* F0, F0 rescued with zebrafish *wars1* mRNA (F0 + zf), F0 rescued with human *WARS1* mRNA (F0 + hm), *wars1* WT sibling (+/+ sib) and homozygous knockout (-/- KO) animals from RNA-seq data. The genes used for heatmap visualization were a set of DEGs in the F0 versus uninjected group. (**F**) Another heatmap visualizes genes involved in aminoacyl-tRNA biosynthesis. (**G** and **H**) Volcano plots for *wars1* F0 versus uninjected control and *wars1*-/- versus *wars1*+/+ sibling animals. Overlapped top DEGs are revealed on the figure. (**I** and **J**) KEGG pathway analysis shows DEGs enrichment in three groups (*wars1* F0 versus uninjected, F0 versus Cas9, and *wars1*-/- versus *wars1*+/+ sibling) and is further divided into upregulation (**I**) and downregulation (**J**) groups. (**K**) Representative images of morphology for uninjected, *med11* F0 and F0 rescued with human *MED11* mRNA at 4 dpf are shown at the left panel. The heatmap at the right panel visualizes 1000 DEGs of uninjected, Cas9-injected, *med11* F0, *med11* F0 rescued with human *MED11* mRNA, *wars1* F0 and *wars1* F0 rescued with human *WARS1* mRNA animals at 3 dpf. Each group contains biological triplicates with six animals in each replicate. Note that one outlier in Cas9 group was removed in (E–J), and another in F0 + *WARS1* group was removed in (**K**). For (A, E-K), the threshold cutoff was set to two-fold change (log2 fold change $\geq \pm 1$) and a *P*-value less than 0.01.

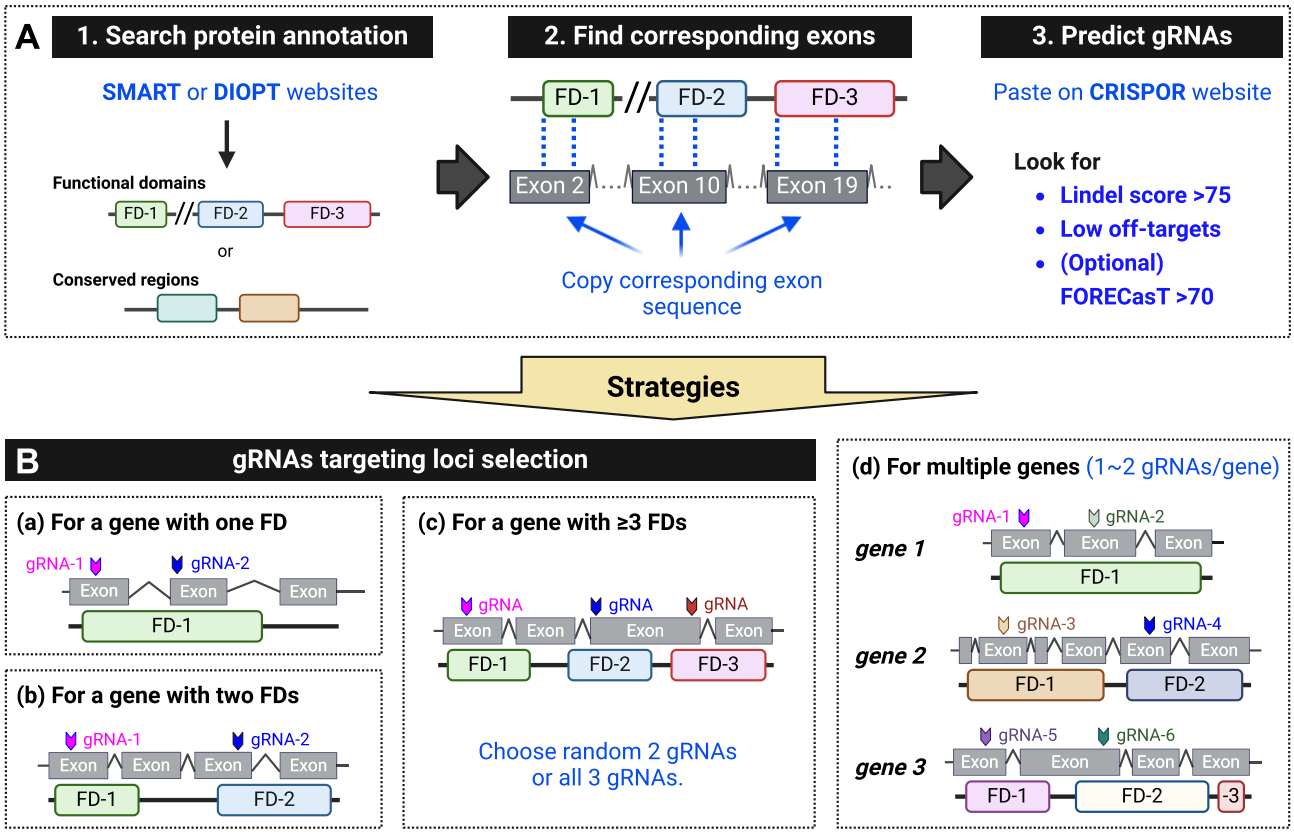

Figure 6. Standardized gRNAs selection and strategies for F0 mutagenesis. (**A**) Steps for finding a gRNA: (1) Identify functional domains (FDs) or conserved regions using resources like the SMART website (http://smart.embl-heidelberg.de/) or the DIOPT database (https://www.flyrnai.org/diopt). (2) Obtain the nucleotide sequence encoding the functional domain. (3) Enter the nucleotide sequence into the CRISPOR website (http://crispor.tefor.net/), select the desired genome and protospacer adjacent motif (PAM), and submit. Prioritize gRNAs with a Lindel score > 75 (outcome score), and as few off-target matches as possible. If no predicted values are shown, extend the input sequence by ~200 base pairs. (**B**) Strategies for designing gRNAs to target loci in various scenarios: (a) For a gene encoding one FD, select two gRNAs: one targeting the beginning of the FD and another targeting the middle. (b) For a gene encoding two FDs, select two gRNAs, each targeting a different domain. (c) For a gene encoding more than three FDs, select two gRNAs targeting any two FDs, or three gRNAs targeting any three FDs. (d) For targeting multiple genes, select one to two gRNAs per gene, targeting FDs. Up to six gRNAs can be co-injected without observed toxicity.

(+/+) (Supplementary Fig. S9B-F). DEGs analysis confirmed this separation, with F0 forming distinct clusters from uninjected, Cas9-injected, rescued, and +/+ sibling samples (Fig. 5E and Supplementary Fig. S10A).

Pathway analysis revealed shared set of genes that were similarly up- or down-regulated in both F0 and stable knockouts (Fig. 5F–J and Supplementary Fig. S10B–F, Supplementary Figs S11–S13). These findings were further validated in knockouts of a second gene, histidyl-tRNA synthetase (*hars*) which exhibited comparable patterns of gene expression changes (Supplementary Fig. S14). Notably, RNA-seq profiles could accurately distinguish F0 knockouts from their controls and rescued groups (Fig. 5K), underscoring the utility of this approach for functional studies. To our knowledge, this represents the first comprehensive RNA-seq analysis of gene-edited zebrafish following phenotypic rescue using mRNA overexpression. Together, these results demonstrate that the phenotypic resemblance between F0 and stable homozygous knockouts is mirrored in their gene expression profiles, validating F0 screening as a reliable proxy for stable knockout approach.

Our data highlight the importance of designing gRNAs with high cutting efficiency and a high likelihood of generating frameshift alleles to achieve efficient biallelic mutations, high penetrance, and low variability. We recommend using prediction tools such as CRISPOR to enhance the probability of generating null mutant-like phenotypes in F0 knockouts (Fig. 6). Contrary to common strategies, targeting early coding exons to induce PTCs was not effective in achieving high phenotype penetrance. Instead, targeting exons encoding the first half of functional domains [9, 10, 12], particularly those with high predicted scores, proved more reproducible and reliable. For larger genes (>3 kb coding), we recommend designing multiple gRNAs targeting different functional domains or conserved amino acid regions to maximize the percentage of animals with null mutant-like phenotypes while minimizing toxicity. These strategies provide a robust framework for generating reliable F0 knockouts that closely mimic stable knockout lines, facilitating rapid and accurate functional genomics studies.

High-throughput F0 analysis demonstrates utility for modeling human disease phenotypes

To demonstrate the utility of our approach for rapid F0 phenotypic analysis across a wide range of tissues and phenotypes, we selected 23 genes and utilized bright-field microscopy, tissue-specific reporter lines, live dyes, and immunohistochemistry to assess phenotypic outcomes in F0 knockouts (Table 1). The genes we targeted included: eight ARS genes implicated in neurological disorders, six genes that cause

Table 1. Summary of expression patterns and loss-of-function phenotypes for each gene in previous studies and this study

Gene symbol	Previous study			This F0 study	
	mRNA expression (ZFIN or PMID)	Tool	Results (PMID)	Phenotypes	Methods
aars1	Brain, eye, liver, pancreas, intestine, and muscle. (34872004)	Morpholino	Motor neuron defect (30124830)	Small brain and eyes, heart edema. Motor neuron defect.	Bright-field & *Tg(olig2:DsRed2;mnx1:EGFP)*
cars1	Brain and eye (ZFIN and 34872004)	ENU	Homozygous mutant fish showed small eye and brain, heart edema (ZFIN)	Small brain and eyes, and heart edema.	Bright-field
gars1	Brain, eye, liver, pancreas, intestine, otic vesicle, and skeletal muscle (34872004)	ENU	Mutants showed small eye and brain, muscle defect and heart edema. (27008886)	Small brain and eyes, and heart edema.	Bright-field
hars	Brain, eye, otic vesicle, liver, and skeletal muscle (31134197)	Morpholino	Knockdown embryos showed small eye and brain, and motor neuron defects. (31134197)	Small brain and eyes, and heart edema.	Bright-field
nars1	Brain, eye, otic vesicle, liver, pancreas, and skeletal muscle (31134197)	–	–	Small brain and eyes, and heart edema.	Bright-field
qars1	Brain, eye, liver, and skeletal muscles (34872004)	CRISPR/Cas9	Homozygous mutant fish showed small eye and brain, and uncoordinated movement. (24656866)	Small brain and eyes, heart edema. Motor neuron defect.	Bright-field & *Tg(olig2:DsRed2;mnx1:EGFP)*
sars1	Brain, eye, liver, and skeletal muscles (34872004)	ENU	Abnormal vascular development. (19423848, 19423847)	Small brain and eyes, heart edema. Motor neuron defect and abnormal vascular development.	Bright-field & *Tg(olig2:DsRed2;mnx1:EGFP & Tg(kdrl:EGFP)*
vars1	Brain, eye, liver, intestine, and skeletal muscles (30755616)	CRISPR/Cas9	Mutants showed small eye and brain, heart edema and seizure like behavior. (30755616)	Small brain and eyes, and heart edema.	Bright-field
MYHs (*myha, myhc4, myhz1.1/1.2/1.3/2*)	Muscles (17537787)	–	–	Short stature and curved body with muscular defect.	Bright-field & Phalloidin staining
slc25a4	Skeletal muscles (ZFIN)	–	–	No obvious morphological abnormality. No obvious heart phenotype. Loosen muscular fibers.	Bright-field & Phalloidin staining
mdh2	Brain, eye and skeletal muscle (ZFIN)	–	–	No obvious morphological abnormality. No obvious muscular structure abnormality.	Bright-field & Phalloidin staining
tpm1	Heart and skeletal muscles (ZFIN)	–	–	Small brain and eyes, no swim bladder, heart defect. Small trunk with muscular defect.	Bright-field & Phalloidin staining
sdha	Brain, eye, liver and skeletal muscles (ZFIN)	–	–	Small brain and eyes. No swim bladder. Curved body with loosen muscular fibers.	Bright-field & Phalloidin staining
lonp1	Brain, eye, otic vesicle, liver, intestine, and skeletal muscles (This study)	–	–	No obvious morphological abnormality. Aberrant muscular structure.	Bright-field & Phalloidin staining
cog1	Brain ventricles and otic vesicle (This study)	–	–	Small head and eye. Aberrant craniofacial features.	Bright-field & Alcian blue staining & *Tg(col2a1a:EGFP-CAAX)*.
mlip	Heart and skeletal muscles (ZFIN)	–	–	No obvious morphological abnormality. Enlarged heart.	Bright-field
setd2	Brain (18231586)	CRISPR/Cas9	Normal blood vessel development (33088589). Note: two sgRNA target sites in previous study, one at very beginning and another at very end of gene.	Abnormal vascular development.	*Tg(kdrl:EGFP)*.
ipo8	–	CRISPR/Cas9	Dorsalization phenotype, cardiovascular and skeletal defects. (34010604)	No obvious morphological abnormality. No obvious muscular structure abnormality. Heart defect and abnormal vascular development.	Bright-field & Phalloidin staining & *Tg(kdrl:EGFP)*
naxe	–	ENU	Liver disease, increased Oil Red O staining. (25950913)	Liver disease	Oil Red O staining
etfa	Brain, eye, liver, and skeletal muscles (ZFIN)	ENU	Liver disease, increased Oil Red O staining. (25950913)	Liver disease	Oil Red O staining
agpat2	Intestine (31950220)	–	–	Liver disease	Oil Red O staining
cyp4v8	Liver and intestinal bulb (ZFIN)	CRISPR/Cas9	Bietti crystalline dystrophy. (35616930)	Liver disease	Oil Red O staining
bscl2	–	–	–	Liver disease	Oil Red O staining

The mRNA expression patterns for each were obtained from published studies (PubMed ID provided) or Zebrafish Information Network, ZFIN (https://zfin.org/). Phenotypes from either morpholino knockdown or ENU (N-ethyl-N-nitrosourea) or CRISPR/Cas9-induced mutagenesis in zebrafish model from previous studies were summarized in the result column. The detailed descriptions of clinical features in humans and phenotypes in mouse knockouts for each gene were included in Supplementary Table S3.

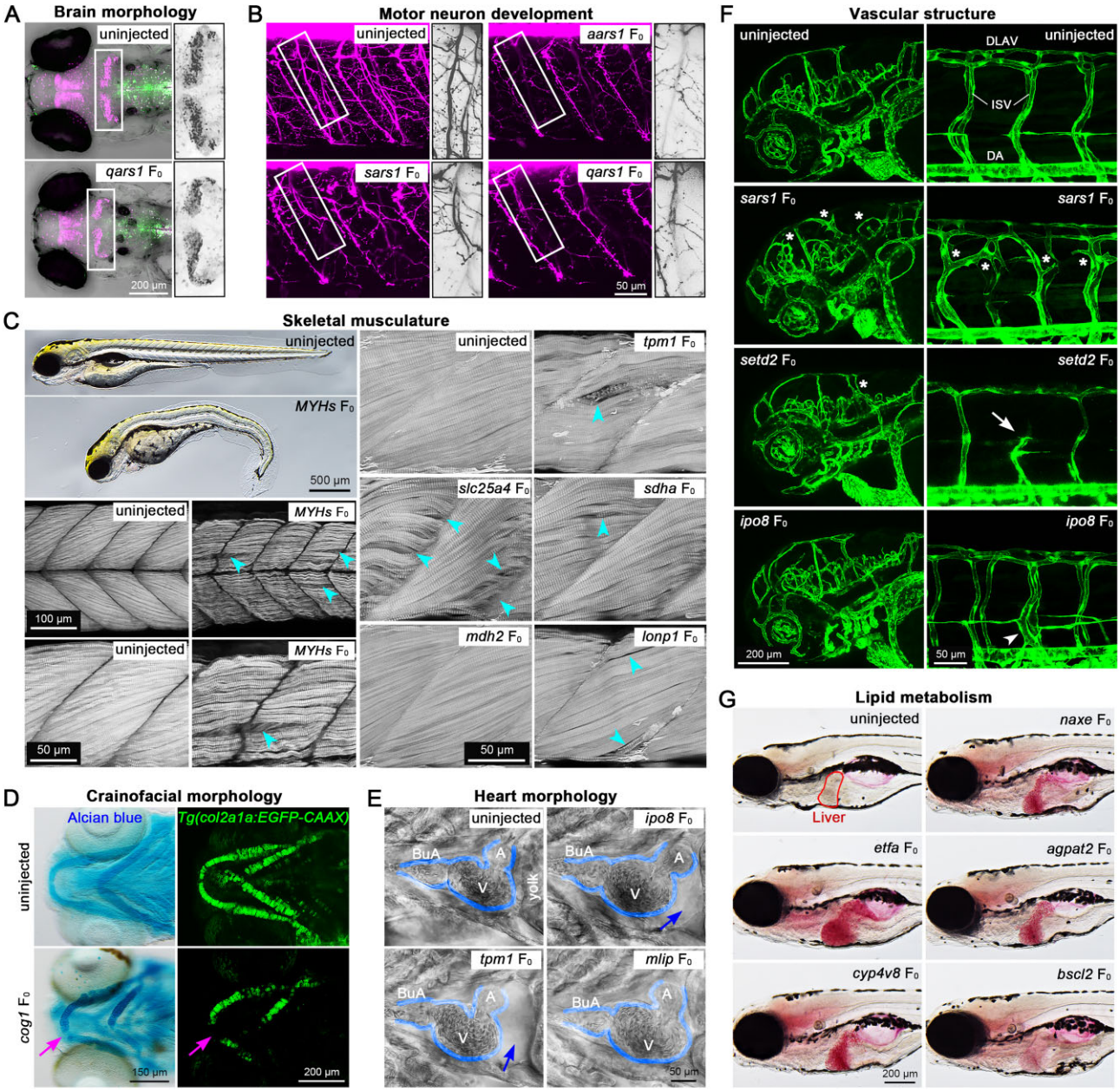

Figure 7. Utilizing the F0 approach to investigate the tissue-specific effects of genes with transgenic reporter lines or through immunohistochemistry. A transgenic line, *Tg(olig2:DsRed2;mnx1:EGFP)*, was used to reveal the morphology of (**A**) the cerebellum (dorsal view; $n = 3$ embryos) and (**B**) motor neurons ($n = 5$ embryos) with red fluorescent protein driven by the *olig2* promoter. (**C**) Fluorescent conjugated phalloidin staining was used to reveal actin filaments in the skeletal muscles of the fish trunk at 10 dpf ($n = 6$ larvae). Blue arrowheads indicate missing (loosened) muscle fibers. (**D**) Alcian blue staining and *Tg(col2a1a:EGFP-CAAX)* was used to reveal the structures of cartilages in *cog1* F0 knockouts at 5 dpf ($n = 10$ larvae). The magenta arrow indicates aberrant cartilage development. A ventral view is shown. (**E**) Bright-field images revealed the cardiac development of animals (n = 4 larvae). The heart was outlined by blue lines, and the blue arrow indicates empty space in pericardium. BuA, bulbus arteriosus; V, ventricle; and A, atrium are indicated. A ventral view is shown. (**F**) Blood vasculature was revealed by *Tg(kdrl:EGFP)* at 5 dpf ($n = 6$ larvae). DLAV, dorsal longitudinal anastomotic vessel; ISV, intersegmental vessel; and DA, dorsal aorta. White asterisks indicate aberrant connected vessel, white arrow indicates defective angiogenesis and the white arrowhead indicates enlarged ISV. (**G**) Oil Red O staining was used to visualize the lipid accumulation in animals at 8 dpf ($n = 35$ larvae). Animals are presented in lateral view, with anterior to the left, unless specifically addressed.

muscular phenotypes, the *cog1* gene implicated in craniofacial morphology, three genes affecting heart development, three genes involved in vasculature, and five lipid metabolism genes.

As expected, *qars1* F0 knockouts showed a reduced cerebellum size (Fig. 7A), while F0 knockouts of *sars1* and *qars1* exhibit abnormal development of motor neurons (Fig. 7B). We observed abnormal muscular development by fluorescent-conjugated phalloidin staining in all six targeted muscular genes: *MYHs* (one gRNA targeting multiple myosin heavy chain genes), *tpm1*, *slc25a4*, *sdha*, *mdh2*, and *lonp1* (Fig. 7C). *cog1* F0s displayed abnormal cartilage development as indicated by either Alcian blue staining or a collagen fluorescent reporter line (Fig. 7D). We also observed abnormal heart development in *tpm1*, *mlip*, and *ipo8* F0 knockouts (Fig. 7E) and aberrant vasculature in *sars1*, *setd2*, and *ipo8* F0 knockouts (Fig. 7F). We used Oil Red O staining for the lipid

Table 2. Summary of genes associated with NDDs, and studies conducted in zebrafish and mouse models

Zebrafish					Human			Mouse	
Gene symbol	Previous study			This F0 study	Gene symbol	Inheritance, Phenotype MIM #	Common phenotypes in patients (PMID)	Gene symbol	Phenotypes in mouse knockout (PMID)
	mRNA expression (ZFIN or PMID)	Tool	Results (PMID)	Phenotypes					
atad3	Brain, eye, otic vesicle, liver, intestine, skeletal muscles, and pronephric ducts (This study)	–	–	Small brain and eyes. No swim bladder. Heart edema. Reduced VSR and AEBR. Increased Oil Red O staining. Aberrant craniofacial feature. Decrease locomotor activity upon LDT.	*ATAD3A*	AD/AR, (617183) AR, (618810)	Axonal neuropathy, optic atrophy or cataracts, seizures, cerebellar atrophy, and hypertrophic cardiomyopathy (28158749); Fatal congenital pontocerebellar hypoplasia (28549128); Hearing loss (28549128); non-alcoholic fatty liver disease (35513069); facial dysmorphism (29053797).	*Atad3a*	Growth retardation, embryos die around embryonic day E7.5. (23372768)
afg2b (*spata5l1*)	Brain ventricles, eye, and otic vesicle (This study)	–	–	Small brain and eyes. No swim bladder. Heart edema. Reduced VSR and AEBR. Increase locomotor activity upon LDT.	*AFG2B* (*SPATA5L1*)	AR (619615, 619616)	Deafness, autosomal recessive 119; NDD with hearing loss and spasticity. Microcephaly, epilepsy, visual impairment, and hearing loss. (34626583)	*Afg2b* (*Spata5l1*)	Embryonic lethal in homozygous. (IMPC)
cox4i1	Brain, eye, liver, skeletal, muscles, and intestine (ZFIN)	–	–	Small brain and eyes. No swim bladder. Heart edema. Short stature. Reduced VSR and AEBR. Decrease locomotor activity upon LDT.	*COX4I1*	AR (619060)	Mitochondrial complex IV deficiency, nuclear type 16. Microcephaly, short stature, developmental delay, visual problem, etc. Leigh syndrome phenotype. (31290619)	*Cox4i1*	Homozygous: embryonic lethal. Heterozygous: abnormal embryo size, abnormal brain development. (IMPC)
cachd1	Brain, eye, otic vesicles, and spinal cord (This study)	CRISPR/ Cas9	Homozygous mutant show craniofacial defect. (38158856)	Craniofacial defect. No swim bladder. Normal VSR. Small otoliths and reduced AEBR. Normal locomotor activity upon LDT.	*CACHD1*	AR (620144)	Rare neurodevelopmental syndrome characterized by variable developmental delay, cognitive impairment and craniofacial dysmorphism. (38158856)	*Cachd1*	Loss-of-function mutations have otoconia deficiencies, hearing and balance impairment. (34388681)
necap1	Brain, eye, otic vesicles, and spinal cord (This study)	–	–	No obvious morphological abnormality. Reduced VSR and AEBR. Small otoliths. Normal locomotor activity upon LDT.	*NECAP1*	AR (615833)	Developmental and epileptic encephalopathy 21	*Necap1*	Embryonic lethal in homozygous. (IMPC) Giant Schnauzer dogs carry homozygous single nucleotide variant display progressive retinal atrophy. (31117272)
sdha	Brain, eye, liver and skeletal muscles (ZFIN)	–	–	Small brain and eyes. No swim bladder. Reduced VSR and AEBR. Decrease locomotor activity upon LDT.	*SDHA*	AR (613642, 252011), AD (619259, 614165)	Cardiomyopathy, dilated, 1GG; Mitochondrial complex II deficiency, nuclear type 1 (Leigh syndrome); Neurodegeneration with ataxia and late-onset optic atrophy; Pheochromocytoma/paraganglioma syndrome 5.	*Sdha*	Embryonic lethal in homozygous. (IMPC)

Table 2. Continued

Zebrafish					Human			Mouse	
Gene symbol	Previous study			This F0 study	Gene symbol	Inheritance, Phenotype MIM #	Common phenotypes in patients (PMID)	Gene symbol	Phenotypes in mouse knockout (PMID)
	mRNA expression (ZFIN or PMID)	Tool	Results (PMID)	Phenotypes					
cog1	Brain ventricles and otic vesicle (This study)	–	–	Aberrant craniofacial features. Small head and eye. Reduced VSR and AEBR. Normal locomotor activity upon LDT.	*COG1*	AR (611209)	Congenital disorder of glycosylation, type Iig. Microcephaly, facial dysmorphism, hearing loss, etc. (19008299)	*Cog1*	Embryonic lethal in homozygous. (IMPC)
yif1b	Whole organism (ZFIN)	–	–	No obvious morphological abnormality. Reduced VSR. Normal AEBR. Normal locomotor activity upon LDT.	*YIF1B*	AR (619125)	Kaya–Barakat–Masson syndrome and Visual impairment. (32006098, 33103737 and 34373908)	*Yif1b*	Knockout mice did not show spontaneous seizures or increased susceptibility to seizures, although mutant mice showed impaired visual perception. Basal locomotion was normal. (33103737)
atn1	–	–	–	No obvious morphological abnormality. Reduced VSR and AEBR. Normal locomotor activity upon LDT.	*ATN1*	AD (618494, 125370)	Congenital hypotonia, epilepsy, developmental delay, and digital anomalies. Dentatorubral-pallidoluysian atrophy. Visual and hearing impairments. (34212383, 36007104)	*Atn1*	Homozygous knockout mice are indistinguishable from WT mice. (17150957)
itsn1	Brain, eye, ear, and skeletal muscle (This study)	–	–	No obvious morphological abnormality. Reduced VSR. Normal AEBR. Decrease locomotor activity upon LDT.	*ITSN1*	NA	Autism spectrum disorders, intellectual disability and epilepsy. (34707297)	*Itsn1*	Homozygous knockout mice display impaired spatial learning and memory. (23447614)
mdh2	Brain, eye, and skeletal muscle (ZFIN)	–	–	No obvious morphological abnormality. Reduced VSR and AEBR. Decrease locomotor activity upon LDT.	*MDH2*	AR (617339)	Developmental and epileptic encephalopathy 51.Early-onset generalized hypotonia, psychomotor delay, refractory epilepsy (34766628). Vision impairment (36420423).	*Mdh2*	Embryonic lethal in homozygous (IMPC).
lonp1	Brain, eye, otic vesicle, liver, intestine, and skeletal muscles (This study)	–	–	No obvious morphological abnormality. Normal VSR. Reduced AEBR. Normal locomotor activity upon LDT.	*LONP1*	AR (600373)	Cerebral, ocular, dental, auricular, and skeletal anomalies (CODAS) syndrome. Developmental delay, craniofacial anomalies, cataracts, hearing loss, short stature, etc. (25574826)	*Lonp1*	Embryonic lethal in homozygous. (25017063)
slc25a4	Skeletal muscles (ZFIN)	–	–	No obvious morphological abnormality. Normal VSR and AEBR. Normal locomotor activity upon LDT.	*SLC25A4*	AD (617184), AR (615418)	Mitochondrial DNA depletion syndrome 12A (cardiomyopathic type); Mitochondrial DNA depletion syndrome 12B (cardiomyopathic type).	*Slc25a4*	Dilated cardiomyopathy. (21232697)
tpm1	Heart and skeletal muscles (ZFIN)	–	–	Small brain and eyes. No swim bladder. Reduced VSR and AEBR.	*TPM1*	AD (611878, 115196)	Cardiomyopathy, dilated, 1Y; Cardiomyopathy, hypertrophic, 3. Atrial septal defect (35243414).	*Tpm1*	Early embryonic lethality of homozygous knockout mouse embryos. (24500875)

Table 2. Continued

Zebrafish					Human			Mouse	
Gene symbol	Previous study			This F0 study	Gene symbol	Inheritance, Phenotype MIM #	Common phenotypes in patients (PMID)	Gene symbol	Phenotypes in mouse knockout (PMID)
	mRNA expression (ZFIN or PMID)	Tool	Results (PMID)	Phenotypes					
qsox1	Brain, liver, otic vesicle, and pronephric duct (ZFIN)	–	–	No obvious morphological abnormality. Normal VSR and AEBR. Decrease locomotor activity upon LDT.	*QSOX1*	NA	–	*Qsox1*	Homozygous knockouts are viable but exhibit moderate dilated cardiomyophathy. (29723491)
ndufa12	Whole organism (This study)	–	–	No obvious morphological abnormality. Reduced VSR and AEBR. Normal locomotor activity upon LDT.	*NDUFA12*	AR (618244)	Mitochondrial complex I deficiency nuclear type 23, including visual impairment and movement disorders. (35141356)	*Ndufa12*	–
phf8	Brain and jaw (20622853); ear and neuromast (33330448)	Morpholino	Brain apoptosis and craniofacial defect (20622853).	No obvious morphological abnormality. Normal VSR and AEBR. Normal locomotor activity upon LDT.	*PHF8*	XLR (300263)	Intellectual developmental disorder, X-linked, syndromic, and Siderius type. Bilateral or unilateral cleft lip/cleft palate. (17661819)	*Phf8*	No obvious developmental defects, no cognitive impairment. With stress-induced anxiety- and depression-like behaviour. (28485378)
aifm1	Brain, eye, liver, and skeletal muscles (ZFIN)	–	–	No obvious morphological abnormality. Reduced VSR and AEBR. Normal locomotor activity upon LDT.	*AIFM1*	XLR (300816, 310490, 300614, 300232)	Combined oxidative phosphorylation deficiency 6; Cowchock syndrome; Deafness, X-linked 5; Spondyloepimetaphyseal dysplasia, X-linked, with hypomyelinating leukodystrophy.	*Aifm1*	Homozygous knockout mice exhibit smaller body size and reduced forebrain. (16788063)
kdm3b	Whole organism (ZFIN)	–	–	No obvious morphological abnormality. Reduced VSR and AEBR. Small otoliths. Decrease locomotor activity upon LDT.	*KDM3B*	AD (618846)	Diets-Jongmans syndrome. Behavioral problems, including ADHD and autism. Hearing loss and low vision. (30929739)	*Kdm3b*	Knockout mice showed restricted postnatal growth and female infertility. (25892958)
thbs1b	Brian, head mesenchyme, eye, otic vesicle, and muscle pioneer (ZFIN)	–	–	No obvious morphological abnormality. Normal VSR and AEBR. Normal locomotor activity upon LDT.	*THBS1*	NA	–	*Thbs1*	Homozygous knockout mice are viable, fertile, and healthy except for lung inflammation and an increase in the number of circulating white blood cells. (9486968)

The mRNA expression patterns for each genes were obtained from published studies (PubMed ID), ZFIN, or this study. The gross morphological phenotypes were determined by observation or measurement after imaging (e.g. Fig. 8E–J, Supplementary Fig. S16F–Y, and Supplementary Fig. S17A and B). The behaviors were summarized from Fig. 8L–N and 8P, Supplementary Fig. S17C and D, and Supplementary Figs S18–S20.
Abbreviations: LDT: light-dark transitions; AR: autosomal recessive; AD: autosomal dominant; NA: not available; VSR: visual startle response; AEBR: acoustic evoked behavioral response; IMPC: International Mouse Phenotyping Consortium; ZFIN: Zebrafish Information Network (https://zfin.org/).

metabolism genes to demonstrate abnormal lipid accumulation in the liver for all five genes (Fig. 7G) [46]. The descriptions for phenotypes for each gene, associated human diseases and previous findings from mouse models are described in Supplementary Table S3. Overall, our data demonstrate that this optimized F0 mutagenesis method together with tissue-appropriate phenotypic readouts can expedite the functional analysis of genes associated with diverse human diseases.

Understanding disease phenotypes often extends beyond gross morphological or tissue-specific phenotypes to include more complex outcomes such as behavioral changes, especially when considering neurodevelopmental disorders (NDDs), including intellectual disability, psychiatric disorders, and deficits in motor skills [64, 65]. While zebrafish are a valuable model for studying NDD-related behaviors [66–68], it has not been thoroughly tested whether F0 mutagenesis is a suitable method for behavioral analysis due to concerns surrounding the potential impact of the injection procedure. To address this question, we compared the visual startle response (VSR), acoustically evoked behavioral response (AEBR), and LDTs of Cas9-injected larvae and uninjected controls. We found no significant differences in any of these behavioral responses (Supplementary Fig. 15A–L), in congruence with our finding that Cas9 injections did not significantly alter gene expression profiles.

Next, we focused on 20 genes linked to NDDs, particularly those causing embryonic lethality in rodents, which has precluded their phenotypic characterization in animal models (Table 2). For each gene, we examined WISH data from the ZFIN database (https://zfin.org) [69] when available, or generated WISH data for the remaining selected genes. Each gene exhibited unique expression patterns, most abundant in the brain (Fig. 8A–D', Supplementary Fig. S16A–E", and Table 2), as would be expected for NDD-associated genes. We generated F0 knockouts for each gene, finding that 6/20 exhibited smaller head and/or eye sizes, 3/20 showed heart edema, and 1/20 had shorter body length (Fig. 8E–J, Supplementary Fig. S16F–Y and Table 2)—all resembling the microcephaly, microphthalmia, cardiomyopathy and short stature found in patients harboring mutations in these genes. Additionally, we observed that *atad3* F0 exhibited abnormal lipid metabolism and craniofacial defects (Supplementary Fig. S17A and B), which are similar to the nonalcoholic fatty liver disease [70] and facial dysmorphism [71] features, respectively, found in *ATAD3A* affected individuals (Table 2).

To assess behavioral phenotypes resulting from each knockout, we placed F0 knockout and control larvae in 96-well plates and recorded their activity after VSR, AEBR, and LDT assays (Fig. 8K). Three of the 20 tested genes (*atad3*, *afg2b* (previously known as *spata5l1*), and *cox4i1*) have been linked to visual or hearing problems in humans [44, 72–74], and we show that their corresponding F0 knockouts displayed similar abnormalities (Fig. 8L). In particular, *atad3* F0 larvae traveled longer during the first minute after light exposure (indicated by blue arrows in Fig. 8M and quantified in Fig. 8N), suggesting a potential light-induced seizure-like behavior [75]. In support of this, *atad3* F0s in a transgenic calcium indicator line showed stronger fluorescence intensity than controls, similar to animals experiencing PTZ-induced seizures (Fig. 8O). However, their overall movement was lower during dark cycles than controls (Fig. 8P), indicating possible movement disabilities. *afg2b* F0 larvae, on the other hand, exhibited a reduction in VSR and AEBR and an increase in distance traveled during the dark period in the more extended 30-minute LDT assay (Fig. 8L, M, and P and Supplementary Fig. S17C and D), which might correlate to the NDD with hearing loss and spasticity (MIM # 619616) in human patients [44].

For the remaining 17 genes we tested, zebrafish F0 larvae recapitulated most of the clinical manifestations observed in human patients for seven genes (*sdha*, *cog1*, *yif1b*, *atn1*, *itsn1*, *mdh2*, and *kdm3b*), while three genes (*lonp1*, *ndufa12*, and *aifm1*) partially recapitulated human phenotypes (Table 2 and Supplementary Figs S18–S20). The phenotypes observed in F0 larvae for three of the genes (*cachd1*, *phf8*, and *thbs1*) were similar to those seen in homozygous knockout mice but have no related reports in patients. For three of the genes (*slc25a4*, *tpm1* and *qsox1*), no NDD-related phenotypes have been documented for either humans or mouse models, but our experiments suggest an abnormal brain and eye morphological phenotypes as well as visual and hearing defects in *tpm1* F0 knockouts and decreased locomotor activity in the LDT assay for *qsox1* F0 knockouts. For the *necap1* F0 larvae, we observed reduced VSR and AEBR as well as small otoliths, whereas previous studies have not found any discernible phenotypes in humans or mouse models. All specific phenotypes from these experiments are shown in Supplementary Figs S18–S20 and summarized in Table 2. Overall, we conclude that our high-throughput F0 mutagenesis approach identified morphological and behavioral abnormalities like those observed in human patients or mouse knockouts, providing a powerful tool for rapidly screening candidate human disease genes associated with different conditions, including NDDs.

F0 phenotype screening for efficient identification of hearing loss-associated genes

Hearing loss is a genetically heterogeneous condition, with over 125 genes implicated in non-syndromic hearing loss predominantly in an autosomal recessive fashion [76]. The zebrafish inner ear is functional by five days post-fertilization and bears striking morphological and genetic similarities with human inner ear [77–80]. In particular, two calcified structures known as otoliths—akin to human otoconia—play a crucial role in transmitting acceleration forces and sound vibrations and can cause hearing or balance disorders if improperly crystallized [81]. Moreover, the zebrafish lateral line system, present along the length of the body and involved in mechanotransduction, is composed of hair cells that bear striking resemblance to those found in the human inner ear (Fig. 9A).

Earlier, we performed transcriptomic studies on adult zebrafish inner ear structures and identified hundreds of genes that were differentially expressed in the utricle (more specialized in horizontal movement related to gravity, vestibular function), saccule (hearing and vertical movement), and lagena (hearing) structures of the inner ear [82, 83]. Additionally, studies using single-cell RNA sequencing (scRNA-seq) on zebrafish lateral line neuromasts have also revealed the diverse functions of hearing-related genes [84, 85]. However, there are some genes exclusively expressed in the cells in zebrafish inner ear but not in lateral line neuromasts [86], or vice versa. This suggests that a comprehensive functional analysis for hearing genes is required. Here we aimed to apply our F0 screening approach (Fig. 9B) to rapidly assess the function of 63 genes identified in these previous transcriptomic studies to

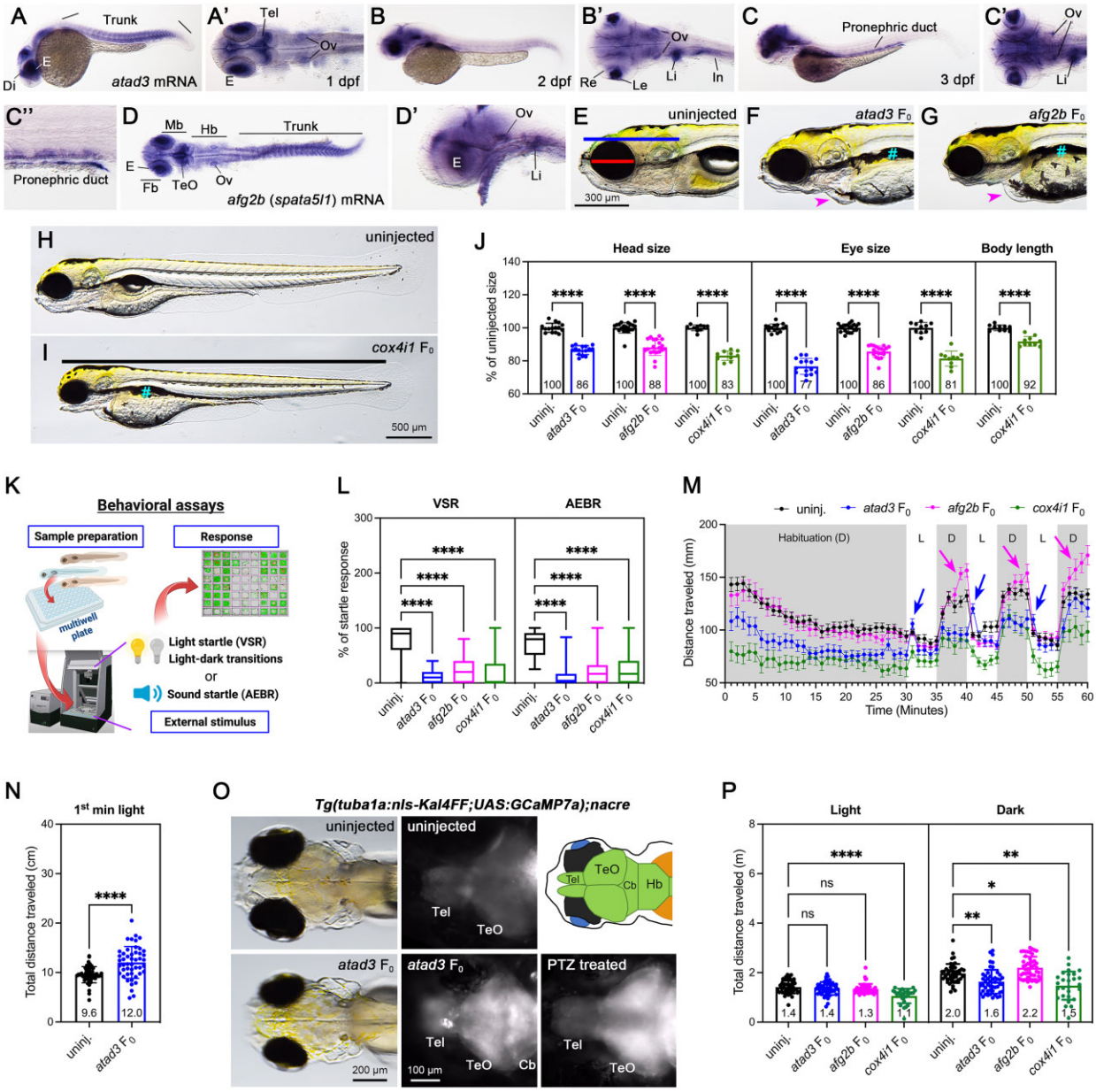

Figure 8. Functional analysis of NDD genes using F0 mutagenesis. (**A**–**D**) WISH method was performed to study mRNA expression patterns for *atad3* at 1 dpf (A, A'), 2 dpf (B, B'), and 3 dpf (C, C', C''), and for *afg2b* at 1 dpf (**D**) and 2 dpf (D'). (A, B, C, and D'), lateral view; and (A', B', C', and D), dorsal view. (**E–I**) Representative images of morphology for uninjected (**E** and **H**), *atad3* (**F**), *afg2b* (**G**), and *cox4i1* (**I**) at 5 dpf. The blue line indicates head size, the red line indicates eye size, the black line indicates body length, magenta arrowheads indicate heart edema, and blue hashtags indicate missing swim bladder. Lateral view and anterior to the left. (**J**) Measurements of head and eye size, and body length of *atad3* ($n = 15$), *afg2b* ($n = 20$), *cox4i1* ($n = 10$) F0 knockouts. (**K**) Experimental procedures were conducted for three behavioral assays on F0 zebrafish larvae. Larvae, with or without injection at 4 dpf, were individually transferred to 96-well plates. The plates were then placed in the behavioral recording chamber on the following day (at 5 dpf) for the LDT test. Subsequently, the plates were moved to an incubator and left for an additional day for the VSR and AEBR assays. The animals' responses to each stimulus and their locomotion were tracked and analyzed using customized software. (**L**) A box and whisker plot was utilized to visualize the percentage of responses in F0 knockouts after VSR and AEBR assays, with a sample size of $n = 24$ larvae for each group. The percentage of responses to five light stimuli for VSR and the responses to 12 sound stimuli for AEBR were calculated for each larva. (**M**) Locomotor activities of zebrafish larvae in LDTs at 5 dpf, $n = 48$ larvae for each group. Larvae were habituated in the dark for 30 min, followed by three cycles of 5-min periods of light and dark. Error bars represent the mean ± SEM. D, dark period, L, light period. Blue arrows indicate the distance moved at the first minute lights on for *atad3* F0 larvae, and magenta arrows indicate the increased distance moved during dark period of *afg2b* F0 larvae. (**N**) Average cumulative distance traveled by each larva during the first minute of the light period as indicated by blue arrow in (**M**). (**O**) Average cumulative distance traveled by each larva during three cycles of either light or dark periods. (**P**) Representative images of the uninjected control and *atad3* F0 in *Tg(tuba1a:nls-Kal4FF;UAS:GCaMP7a);nacre* under bright-field (left panel) and fluorescent microscopy (middle panel) at 5 dpf. The schematic diagram illustrates the structure of the zebrafish larva brain at the top right panel, while the bottom right panel displays a fluorescent image of uninjected larvae treated with 15 mM pentylenetetrazole (PTZ) at 5 dpf. $n = 3$ larvae for each group. Dorsal view, anterior to the left. For (**J**, **N**, and **O**), each dot represents one larva, and error bars indicate the mean ± SD. For (**J**, **L**, and **O**), statistical significance was calculated by Brown–Forsthye and Welch's ANOVA with Dunnett's T3 multiple comparisons test; for (**N**), two-tailed unpaired Student's *t* test with Welch's correction: not significant (ns) $P \geq 0.05$, $^{*}P < 0.05$, $^{**}P < 0.01$, and $^{****}P < 0.0001$. Di, diencephalon; E, eye; Tel, telencephalon; Ov, otic vesicle; Re, retina; Le, lens; Li, liver; In, intestine; Fb, forebrain; Mb, midbrain; Hb, hindbrain; TeO, optic tectum; Cb, cerebellum.

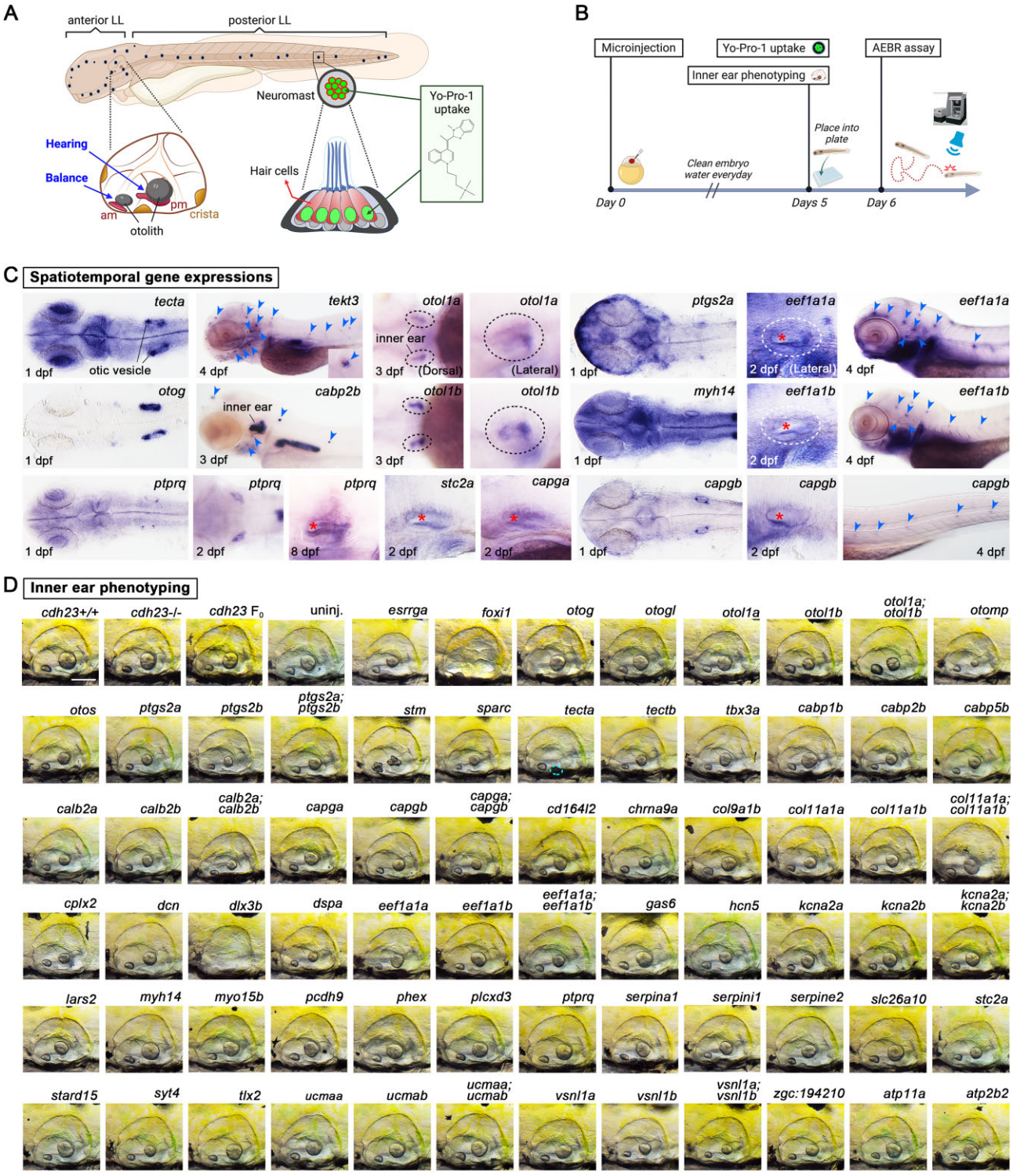

Figure 9. Screening for genes involved in hearing and vestibular function by F0 approach. (**A**) The cartoon figure illustrates zebrafish larval sensory systems, including the inner ear and the neuromast in the lateral line. The inner ear contains the anterior macula (am) with an otolith attached to the ciliary bundles of macular hair cells, responsible for balance, and the posterior macula (pm) with an otolith attached to the ciliary bundles of macular hair cells, responsible for hearing. Additionally, there are three cristae for sensing angular rotation. Functional (mechanotransduction) and viable hair cells in the lateral line neuromast can uptake live nuclear dyes such as Yo-Pro-1. (**B**) A hearing gene screening pipeline was established. Embryos, both with and without microinjection, were rinsed with embryo water daily until 5 dpf for inner ear phenotyping and Yo-Pro-1 uptake experiments. The remaining larvae were individually transferred to 96-well plates for the AEBR assay at 6 dpf. (**C**) The WISH method was performed to study mRNA expression patterns for hearing genes. The blue arrowheads indicate the lateral line neuromast, the dashed close circle indicates the inner ear, and the red asterisk indicates the sensory epithelium in the inner ear. Stained embryos at 1 dpf for all genes, at 3 dpf for *otol1a* and *otol1b* in the left panel, and at 2 dpf for *ptprq* were displayed in dorsal view. The rest were shown in lateral view, with the anterior to the left. (**D**) Representative images of inner ear morphology for each F0 knockout. Scale bar = 0.1 mm. Lateral view with the anterior to the left.

investigate their role in inner ear and lateral line development and function.

First, we verified the expression of selected genes for the screen in hearing related tissues by analyzing publicly available databases including scRNA-seq from the mouse cochlear epithelium and zebrafish neuromast (https://umgear.org/), and ZFIN to gather the spatial and/or temporal gene expression profiles that corelate with hearing function. For genes lacking expression data in these datasets, we performed WISH to visualize their tissue distribution. We used known genes such as *tecta* and *otog* (otic vesicle), *otol1a* (inner ear), *tekt3* and *capgb* (lateral line neuromasts), and *cabp2b* (both inner ear and neuromasts) as positive controls (Fig. 9C). This analysis revealed 13 genes that were previously not known to be highly expressed in hearing-related tissues. Notably, some duplicated genes displayed similar expression patterns (e.g. *otol1a*/*otol1b*, *eef1a1a*/*eef1a1b*, and *vsnl1a*/*vsnl1b*) (Fig. 9C, Supplementary Fig. S21, and Supplementary Table S4).

Next, we generated F0 knockouts for 62 genes, including single knockouts for each gene and double knockouts for duplicated genes (total of 71 injected groups), and assessed inner ear morphological phenotypes. We compared these observations to previously published stable knockouts, including *foxi1*-/- (*quadro*^{m271}) [87], *otog*-/- (*eis*^{te296f}) [88] and *tecta*-/- (*rst*^{tl20e}) [88] as positive controls. We observed aberrant otolith phenotype in 33 injected groups, including three F0s corresponding to the positive controls and seven genes that were previously implicated in otolith formation using morpholino knockdown (*esrrga* [89], *otomp* [90], *ptgs2a* [91], *stm* [92], *sparc* [93], *tectb* [94], and *dlx3b* [95]) (Fig. 9D and Supplementary Table S4). Additionally, we found that F0 knockouts of five genes (*otos*, *tbx3a*, *capgb*, *dcn*, and *dspa*) showed aberrant otolith phenotypes that were previously undescribed. In contrast to previous studies [90, 96], we found that F0 kncokouts in two genes (*otogl* and *otol1a*) showed normal otoliths. Altogether, 22 novel genes (Supplementary Table S4) and one double F0 knockout (*eef1a1a;eef1a1b*) showed abnormal otolith phenotypes in our screen (Fig. 9D).

For each single or double F0 knockout, we assessed hair cell development and function using the Yo-Pro-1 uptake assay [42] and compared to *cdh23*-/- and *cdh23* F0 (defective mechanotransduction) and *capgb* F0 (defective hair cell development) animals as positive controls. As expected, both the *cdh23*-/- knockouts and F0s displayed a complete absence of Yo-Pro-1 + hair cells (Fig. 10A and B) while the *capgb* F0s showed a significant reduction in Yo-Pro-1 + hair cells. Of the 71 injected groups, 38 exhibited aberrant Yo-Pro-1 uptake, including 32 single F0s, six double F0s containing one or more of the single-gene hits, and one double knockout (*ptgs2a;ptgs2b*) composed of two genes that did not display a phenotype on their own (Fig. 10A and B, Supplementary Figs S22 and S23, and Supplementary Table S4). In addition to this set of F0s, we also assayed an F0 knockout of a mature hair cell-specific gene, *tekt3* [97] (Fig. 9C), and found a significant reduction in the number of Yo-Pro-1 + hair cells (Fig. 10A and B), further suggesting its role in hair cell development.

To measure hearing function, we performed the AEBR assay – in which zebrafish larvae are exposed to sudden sound stimuli and their movement following each stimulation is recorded—on the 71 injected groups of F0 animals. 19 injected groups (including 18 single gene F0 knockouts and one double F0 knockout (*capga;capgb*)) showed a reduction in their hearing startle responses (Fig. 10C, Supplementary Figs S24 and S25, and Supplementary Table S4). Interestingly, we found six F0 knockouts that showed neither otolith morphology nor Yo-Pro-1 uptake phenotypes but exhibited aberrant AEBR. Two of these genes (*tlx2* and *pcdh9*) are expressed in the statoacoustic ganglion, and another two (*otogl* and *col9a1)* have been implicated in mouse tectorial membrane morphology [98, 99].

In summary, our F0 screening approach rapidly identified abnormalities in 52 out of 63 individual genes with known hearing-related functions, recapitulating the phenotypes observed in stable knockout lines and morpholino knockdown animals. We also uncovered three pairs of duplicated genes that exhibited phenotypes when both paralogs were targeted, but not when each was disrupted on its own. We used this rapid approach to discover many previously unknown phenotypes, including 22 F0s with aberrant otoliths, 32 F0s with abnormal Yo-Pro-1 uptake, and 19 F0s with abnormal hearing startle responses. Notably, the *otol1b* F0 as well as *otol1a;otol1b* F0 knockouts displayed an enlarged anterior otolith with vestibular dysfunction but normal hearing (Fig. 9D and 10C and Supplementary Video 1, Supplementary Video 2), which is an unusual outcome that merits further investigation [83, 100, 101].

Investigation of genetic compensation in F0 and stable knockouts

Genetic knockouts in animal models are essential for studying gene function, but they do not always accurately reflect human diseases. For example, recent studies have shown significant differences in hearing loss severity between human patients and genetically modified mice for approximately half of the genes tested [102–105]. Similarly, many single-gene zebrafish knockouts exhibit mild or no phenotypes, unlike their morpholino-mediated gene knockdown counterparts [106]. Recent studies suggest genetic compensation, also known as transcriptional adaptation, is a phenomenon where the loss of function of one gene leads to the upregulation of related genes, potentially masking the phenotypic effects of the mutation could explain this discrepancy in both zebrafish and mice [58, 59, 107, 108]. Although some studies indicate that zebrafish F0 knockouts might circumvent this genetic compensation mechanism observed in stable knockout lines [108–110], the relationship between F0 knockouts and genetic compensation remains an area of active investigation. To explore this further, we compared the phenotypes and gene expression profiles of F0 knockouts and stable mutant lines for several genes associated with hearing loss. In our previous work, we generated a library of knockouts for genes associated with non-syndromic hearing loss and found that some stable knockouts accurately recapitulate hearing-associated phenotypes, while others displayed mild or no phenotypes [7]. To determine whether genetic compensation could be playing a role in some of these stable knockout lines, we used the AEBR assay to compare hearing startle responses between F0 and stable knockouts for six hearing-related genes.

First, we used *msrb3* and *tmprss3a;tmprss3b* double knockouts, both these stable knockouts show hearing defects in our hands [7], with *TMPRSS3* as an example of a duplicated gene in zebrafish, and *Msrb3* as an example of a genetic compensation found in mouse model [111]. F0 knockouts for *msrb3*

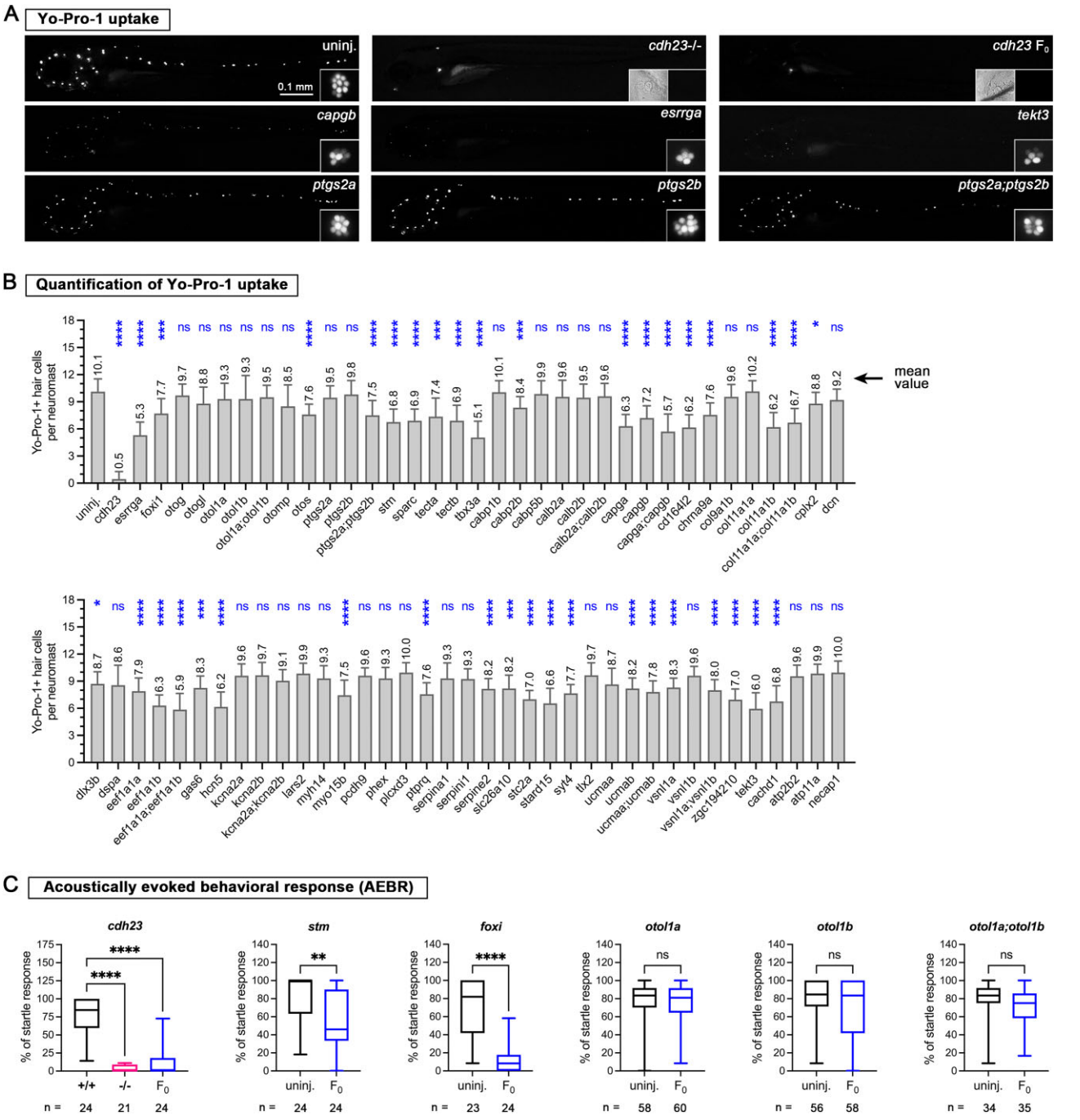

Figure 10. High-throughput hearing gene screening in F0 knockouts using Yo-Pro-1 and acoustic evoked behavior response (AEBR) assay. (**A**) Representative fluorescent images of Yo-Pro-1 uptake for each F0 with an enlarged image of a neuromast placed in the bottom right corner. The images are shown in lateral view with the anterior to the left. A homozygous *cdh23* knockout *(cdh23-/-)* was used as a positive control for the hearing loss phenotype. For example, neuromast morphology can be observed under bright-field, but no Yo-Pro-1-positive (Yo-Pro-1+) cells are present. Images for other hearing genes were presented in Supplementary Fig. S22 and Supplementary Fig. S23. (**B**) Quantification of the average number of Yo-Pro-1+ cells per neuromast ($n = 4$ neuromasts) of each F0 knockout ($n = 5$ larvae). Since the average number of Yo-Pro-1 + cells per neuromast was around 10 cells for uninjected controls across multiple experiments, we combined all numbers ($n = 45$ larvae). Error bars indicate the mean ± SD. Statistical significance was compared to the uninjected control group and calculated by Brown–Forsthye and Welch's ANOVA with Dunnett's T3 multiple comparisons test: not significant (ns) $P \geq 0.05$, $^{*}P < 0.05$, $^{***}P < 0.001$, and $^{****}P < 0.0001$. (**C**) A stable homozygous *cdh23* knockout (*cdh23-/-*) was used as a positive control for the hearing loss phenotype. The AEBR assay results for other hearing genes were presented in Supplementary Fig. S24 and Supplementary Fig. S25. The percentage of responses to 12 sound stimuli for AEBR was calculated for each larva using AEBR. Statistical significance was determined using two-tailed unpaired Student's *t* test with Welch's correction: not significant (ns) $P \geq 0.05$, $^{*}P < 0.05$, $^{**}P < 0.01$, $^{***}P < 0.001$, and $^{****}P < 0.0001$ compared to uninjected controls from the same batch.

and *tmprss3* displayed phenotypes similar to those of stable knockouts (Fig. 11A and B), suggesting genetic compensation may not be a factor in these cases. However, we did observe an upregulation of *msrb1a*, *msrb1b*, and *msrb2* in *msrb3*-/- knockouts. Next, we selected four stable knockouts (*coch, tbc1d24, pou4f3*, and *gipc3*), which their mutations cause hearing loss in humans [112–115] but zebrafish knockouts don't show obvious hearing defects in our hands. Results showed that F0 knockouts in all four genes did not exhibit any evident hearing defects (Fig. 11C–F) as observed in their stable knockouts, suggesting genetic compensation may also not be a factor in these cases.

To determine whether genetic compensation could explain the lack of phenotype in these mutants, we explored the role of the NMD pathway, which has been implicated in triggering genetic compensation. Recent studies have shown that PTC-bearing mRNAs can induce upregulation of related genes through a mechanism involving the NMD pathway and the COMPASS complex. Our previous data, along with published reports, suggest that suppressing components of the UPF pathway (UPF3 or UPF1) can block genetic compensation [107, 108, 116]. Here we targeted the double F0 knockouts of *upf3a* and *upf3b* due to their partial redundancy [116] and to avoid the behavioral effect observed in *upf1* knockout (Supplementary Fig. S26). Notably, knocking down *UPF3* paralogs in *msrb3*-/- reduced their hearing startle responses; however, stable knockouts for *coch*, *tbc1d24*, *pou4f3*, and *gipc3* did not exhibit any hearing phenotype (Fig. 11C–F). These findings suggest that genetic compensation is unlikely to explain the lack of phenotype observed in these specific knockouts.

Taken together, our results suggest that the absence of a disease-related phenotype in stable knockouts may not always be due to genetic compensation, and it is not a universal phenomenon in the zebrafish model system.

Discussion

Functional validation of human disease-associated genes remains a critical bottleneck in understanding and predicting genetic disorders. Traditional approaches often necessitate time- and resource-intensive multigenerational breeding schemes in gene-edited model organisms [7]. Zebrafish offer a compelling platform for rapid phenotypic characterization of disease genes in the F0 generation, but the scalability of such studies has been hindered by challenges including low phenotypic penetrance, potential toxicity and off-target editing, high variability, and possible genetic redundancy and/or compensation [117–121].

In this study, we present a systematically tested and optimized approach to F0 CRISPR/Cas9 mutagenesis in zebrafish, enabling, high-throughput screening functional validation of candidate human disease genes with high phenotype penetrance. Our approach faithfully recapitulates pathophysiological phenotypes and gene expression changes observed in stable knockout lines, which typically takes months to generate [43]. Through the systematic evaluation of 324 gRNAs targeting 125 genes, we demonstrate the robustness of this approach for analyzing disease genes affecting various tissues. Our successful identification of previously uncharacterized impacts of genes implicated in NDDs and hearing abnormalities underscores the potential of our F0 screening method to uncover novel genetic functions and interactions in a high-throughput and efficient manner, particularly in the context of polygenic traits and diseases.

Various groups have refined F0 mutagenesis protocols in zebrafish using different modifications such as *in vitro*-transcribed (IVT) gRNA co-injected with Cas9 mRNA or Cas9 protein [5, 8], dgRNA (crRNA/tracrRNA) with Cas9 protein, or chemically synthesized single gRNA with Cas9 protein [9]. We recommend synthetic gRNAs (either single or dual) due to limitations inherent in the use of T7 RNA polymerase for IVT gRNA synthesis, which necessitates adherence to the 5′-GG $(N)_{18}$NGG-3′ rule to ensure high-quality and efficient editing [5]. This constraint reduces the flexibility of selecting gRNAs with optimal scores. While IVT gRNAs are not inherently less effective than synthetic gRNAs, the addition of extra G or GG at the 5′ end significantly reduces editing efficiency [7, 122]. Conversely, IVT gRNAs that retain the original 5′-GG exhibit similar editing efficiencies to synthetic gRNAs (see Fig. 1F in Hoshijima *et al.* 2019) [9]. For this study, we selected gRNA target sequences containing at least one G at the first two bases of the 5′ end, replacing non-G bases with G when necessary. In certain cases, we replaced 5′-NN with GG during gRNA selection (e.g. Fig. 1A: *noto*_2 and Fig. 1B: *rx3*_8), yet consistently achieved > 80% phenotypic penetrance (and often > 90%) with robust phenotypes [5, 7, 122].

The utility of our method is exemplified through the phenotypic validation of numerous human disease genes across diverse tissues. By targeting genes implicated in NDDs, hearing loss, and metabolic diseases, we uncovered previously uncharacterized phenotypes, many of which recapitulate clinical manifestations in human patients. For example, our findings on *atad3* and *afg2b* F0 knockouts provide new insights into the pathophysiology of these genes, underscoring the translational potential of F0 mutagenesis. Furthermore, the ability to investigate polygenic traits through multiplexed F0 knockouts highlights the adaptability of this approach for studying complex genetic interactions and epistasis.

Our findings suggest that genetic compensation is not a universal phenomenon and may vary depending on the specific gene and genetic background. The observation that some F0 knockouts and stable mutants show similar phenotypes indicates that F0 screening can be a valuable tool for rapid assessment of gene function. However, the lack of phenotypes in both F0 and stable knockouts for some hearing-related genes highlights the complexity of genetic networks and the potential limitations of single-gene knockout approaches. These results emphasize the importance of considering alternative mechanisms that may explain the absence of expected phenotypes in knockout models. Future studies should explore the role of other NMD components and epigenetic factors in genetic compensation, the potential for combinatorial gene knockouts to reveal masked phenotypes, the use of more sensitive phenotyping methods to detect subtle functional changes, and the investigation of potential species-specific differences in genetic compensation mechanisms between zebrafish and mammals.

Adopting this optimal gRNA selection process not only increases the likelihood of generating loss-of-function models, but it may simplify the workflow, making the guide selection and evaluation of the model more scalable. Assuming this can achieve gains in model generation with fewer guides and less time spent selecting a model, adopting this robust workflow enables small-to-medium scale screening of 50–500 genes with ease. For instance, human microdeletions—small chromoso-

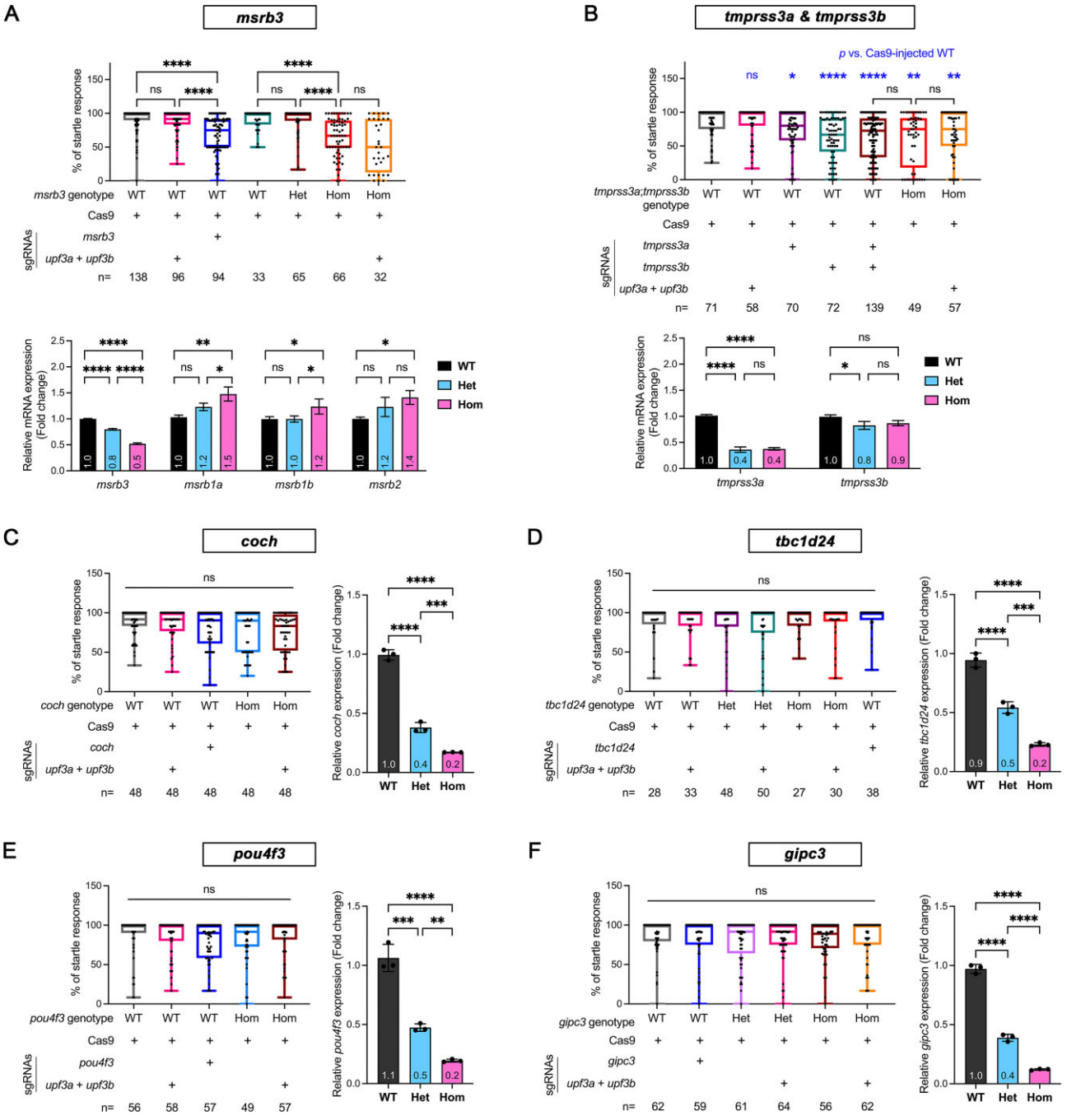

Figure 11. Investigation of genetic compensation by inactivating *upf3* paralogs in stable knockouts of hearing genes. (**A**) The *msrb3* F0 knockouts exhibited a reduced AEBR compared to either Cas9-injected or *upf3a;upf3b* F0 knockout larvae. Similarly, *msrb3* homozygous (Hom) knockouts showed a reduced AEBR compared to either WT or heterozygous (Het) larvae. RT-qPCR showed a significant reduction in *tmprss3a*, whereas *tmprss3b* was slightly reduced in both *tmprss3a;tmprss3b* heterozygous and homozygous knockouts. (**B**) The *tmprss3a* F0, *tmprss3b* F0, *tmprss3a;tmprss3b* F0, *tmprss3a*^{Hom}*;tmprss3b*^{Hom} and *tmprss3a*^{Hom}*;tmprss3b*^{Hom} coinjected with *upf3a* and *upf3b* gRNAs (*tmprss3a*^{Hom}*;tmprss3b*^{Hom}*;upf3a;upf3b* F0) showed a reduced AEBR compared to Cas9-injected larvae. Furthermore, *tmprss3a;tmprss3b* F0, *tmprss3a*^{Hom}*;tmprss3b*^{Hom}, and *tmprss3a*^{Hom}*;tmprss3b*^{Hom}*;upf3a;upf3b* F0 larvae exhibited a similar degree of reduction in AEBR assay. RT-qPCR showed a significant reduction in *tmprss3a*, whereas *tmprss3b* was slightly reduced in both *tmprss3a;tmprss3b* heterozygous and homozygous knockouts. (**C**-**F**) Comparisons of the AEBR assay for control versus F0, stable knockout, and stable knockout coinjected with *upf3a* and *upf3b* gRNAs in *coch* (**C**), *tbc1d24* (**D**), *pou4f3* (**E**), and *gipc3* (**F**) genes showed no difference. RT-qPCR analysis was performed to determine the gene expression levels in each knockout, and the results are shown in the right panel. Each group was compared with every other group. The percentage of responses to 12 sound stimuli for AEBR were calculated for each larva. Statistical significance was calculated by Brown–Forsythe and Welch's ANOVA with Dunnett's T3 multiple comparisons test: not significant (ns) $P \geq 0.05$, $^{*}P < 0.05$, $^{**}P < 0.01$, $^{***}P < 0.001$, and $^{****}P < 0.0001$.

mal deletions associated with various rare diseases—often span multiple genes within a region. Wetzel *et al*. reported over 250 such microdeletions identified in humans [123]. Using this approach, it will be possible to efficiently screen many genes in parallel. Given the multiplexing capabilities of this approach, it will be possible to knock out genes in combination with other genes within a microdeletion region.

Moving forward, the scalability of this method could be enhanced further through automation and integration with high-throughput phenotyping [124] or screening, such as Multiplexed Intermixed CRISPR Droplets (MIC-Drop) platforms [125]. Additionally, expanding this pipeline to other model organisms could facilitate cross-species comparisons and the identification of conserved genetic pathways. In conclusion, our study establishes a robust and scalable framework for the functional analysis of human disease genes by comparing various gRNA selection tools and knockout approaches while highlighting best practices for selecting efficient guides.

Acknowledgements

We thank Ruth Clark and the Comparative Medicine Department for animal care. We thank Dr. Karen Mruk (East Carolina University), Dr. Ryan S Gray (University of Texas, Austin), Dr. Philippe Mourrain (Stanford University), and Zebrafish International Resource Center (ZIRC) for sharing transgenic reporter lines. We also thank Dr. Shawn Burgess (NHGRI/NIH) for his critical feedback and suggestions.

Author contributions: S.J.L. (Conceptualization [equal], Data curation [lead], Formal analysis [lead], Investigation [lead], Methodology [equal], Validation [lead], Visualization [lead], and Writing—original draft [lead]), K.H. (Formal analysis [supporting], Investigation [supporting], and Methodology [supporting]), C.P. (Investigation [supporting] and Methodology [supporting]), W.Q. (Investigation [supporting] and Methodology [supporting]), P.V. (Investigation [supporting] and Methodology [supporting]), and G.K.V. (Conceptualization [lead], Data curation [equal], Formal analysis [lead], Funding acquisition [lead], Project administration [lead], Resources [lead], Supervision [lead], Validation [lead], Visualization [lead], and Writing - original draft [lead]).

Supplementary data

Supplementary data is available at NAR online.

Conflict of interest

None declared.

Funding

This work was supported by the US National Institutes of Health (NIH) [grants, R21DC020317, and ORIP R24OD034438 (GKV)]. Funding to pay the Open Access publication charges for this article was provided by the National Institutes of Health, and Oklahoma Medical Research Foundation.

Data availability

The data underlying this article will be shared upon request. The raw data for RNA sequencing and NGS are available in the NCBI Sequence Read Archive (SRA) under the accession number PRJNA1123309.

References

1. Ewans LJ, Minoche AE, Schofield D *et al.* Whole exome and genome sequencing in mendelian disorders: a diagnostic and health economic analysis. *Eur J Hum Genet* 2022;**30**:1121–31. https://doi.org/10.1038/s41431-022-01162-2
2. Baldridge D, Wangler MF, Bowman AN *et al.* Model organisms contribute to diagnosis and discovery in the undiagnosed diseases network: current state and a future vision. *Orphanet J Rare Dis* 2021;**16**:206. https://doi.org/10.1186/s13023-021-01839-9
3. Holtzman NG, Iovine MK, Liang JO *et al.* Learning to fish with genetics: a primer on the vertebrate model Danio rerio. *Genetics* 2016;**203**:1069–89. https://doi.org/10.1534/genetics.116.190843
4. Howe K, Clark MD, Torroja CF *et al.* The zebrafish reference genome sequence and its relationship to the human genome. *Nature* 2013;**496**:498–503. https://doi.org/10.1038/nature12111
5. Gagnon JA, Valen E, Thyme SB *et al.* Efficient mutagenesis by Cas9 protein-mediated oligonucleotide insertion and large-scale assessment of single-guide RNAs. *PLoS One* 2014;**9**:e98186. https://doi.org/10.1371/journal.pone.0098186
6. Jao LE, Wente SR, Chen W. Efficient multiplex biallelic zebrafish genome editing using a CRISPR nuclease system. *Proc Natl Acad Sci USA* 2013;**110**:13904–9. https://doi.org/10.1073/pnas.1308335110
7. Varshney GK, Pei W, LaFave MC *et al.* High-throughput gene targeting and phenotyping in zebrafish using CRISPR/Cas9. *Genome Res* 2015;**25**:1030–42. https://doi.org/10.1101/gr.186379.114
8. Burger A, Lindsay H, Felker A *et al.* Maximizing mutagenesis with solubilized CRISPR-Cas9 ribonucleoprotein complexes. *Development* 2016;**143**:2025–37.
9. Hoshijima K, Jurynec MJ, Klatt Shaw D *et al.* Highly efficient CRISPR-Cas9-based methods for generating deletion mutations and F0 embryos that lack gene function in zebrafish. *Dev Cell* 2019;**51**:645–57. https://doi.org/10.1016/j.devcel.2019.10.004
10. Kroll F, Powell GT, Ghosh M *et al.* A simple and effective F0 knockout method for rapid screening of behaviour and other complex phenotypes. *eLife* 2021;**10**:e59683. https://doi.org/10.7554/eLife.59683
11. Shah AN, Davey CF, Whitebirch AC *et al.* Rapid reverse genetic screening using CRISPR in zebrafish. *Nat Methods* 2015;**12**:535–40. https://doi.org/10.1038/nmeth.3360
12. Wu RS, Lam II, Clay H *et al.* A rapid method for directed gene knockout for screening in G0 Zebrafish. *Dev Cell* 2018;**46**:112–25. https://doi.org/10.1016/j.devcel.2018.06.003
13. Uribe-Salazar JM, Kaya G, Sekar A *et al.* Evaluation of CRISPR gene-editing tools in zebrafish. *BMC Genomics* 2022;**23**:12. https://doi.org/10.1186/s12864-021-08238-1
14. Naert T, Tulkens D, Edwards NA *et al.* Maximizing CRISPR/Cas9 phenotype penetrance applying predictive modeling of editing outcomes in Xenopus and zebrafish embryos. *Sci Rep* 2020;**10**:14662. https://doi.org/10.1038/s41598-020-71412-0
15. Moreno-Mateos MA, Vejnar CE, Beaudoin JD *et al.* CRISPRscan: designing highly efficient sgRNAs for CRISPR-Cas9 targeting in vivo. *Nat Methods* 2015;**12**:982–8. https://doi.org/10.1038/nmeth.3543
16. Bae S, Kweon J, Kim HS *et al.* Microhomology-based choice of Cas9 nuclease target sites. *Nat Methods* 2014;**11**:705–6. https://doi.org/10.1038/nmeth.3015
17. Chen W, McKenna A, Schreiber J *et al.* Massively parallel profiling and predictive modeling of the outcomes of CRISPR/Cas9-mediated double-strand break repair. *Nucleic Acids Res* 2019;**47**:7989–8003. https://doi.org/10.1093/nar/gkz487

18. Labun K, Montague TG, Krause M *et al.* CHOPCHOP v3: expanding the CRISPR web toolbox beyond genome editing. *Nucleic Acids Res* 2019;**47**:W171–4. https://doi.org/10.1093/nar/gkz365
19. Shen MW, Arbab M, Hsu JY *et al.* Predictable and precise template-free CRISPR editing of pathogenic variants. *Nature* 2018;**563**:646–51. https://doi.org/10.1038/s41586-018-0686-x
20. Allen F, Crepaldi L, Alsinet C *et al.* Predicting the mutations generated by repair of Cas9-induced double-strand breaks. *Nat Biotechnol* 2019;**37**:64–72. https://doi.org/10.1038/nbt.4317
21. LaFave MC, Varshney GK, Vemulapalli M *et al.* A defined zebrafish line for high-throughput genetics and genomics: NHGRI-1. *Genetics* 2014;**198**:167–70. https://doi.org/10.1534/genetics.114.166769
22. Beis D, Bartman T, Jin SW *et al.* Genetic and cellular analyses of zebrafish atrioventricular cushion and valve development. *Development* 2005;**132**:4193–204. https://doi.org/10.1242/dev.01970
23. Dale RM, Topczewski J. Identification of an evolutionarily conserved regulatory element of the zebrafish col2a1a gene. *Dev Biol* 2011;**357**:518–31. https://doi.org/10.1016/j.ydbio.2011.06.020
24. Leung LC, Wang GX, Madelaine R *et al.* Neural signatures of sleep in zebrafish. *Nature* 2019;**571**:198–204. https://doi.org/10.1038/s41586-019-1336-7
25. Letunic I, Bork P. 20 years of the SMART protein domain annotation resource. *Nucleic Acids Res* 2018;**46**:D493–6. https://doi.org/10.1093/nar/gkx922
26. Letunic I, Khedkar S, Bork P. SMART: recent updates, new developments and status in 2020. *Nucleic Acids Res* 2021;**49**:D458–60. https://doi.org/10.1093/nar/gkaa937
27. Hu Y, Comjean A, Rodiger J *et al.* FlyRNAi.Org-the database of the Drosophila RNAi screening center and transgenic RNAi project: 2021 update. *Nucleic Acids Res* 2021;**49**:D908–15. https://doi.org/10.1093/nar/gkaa936
28. Hu Y, Flockhart I, Vinayagam A *et al.* An integrative approach to ortholog prediction for disease-focused and other functional studies. *BMC Bioinf* 2011;**12**:357. https://doi.org/10.1186/1471-2105-12-357
29. Concordet JP, Haeussler M. CRISPOR: intuitive guide selection for CRISPR/Cas9 genome editing experiments and screens. *Nucleic Acids Res* 2018;**46**:W242–5. https://doi.org/10.1093/nar/gky354
30. Doench JG, Fusi N, Sullender M *et al.* Optimized sgRNA design to maximize activity and minimize off-target effects of CRISPR-Cas9. *Nat Biotechnol* 2016;**34**:184–91. https://doi.org/10.1038/nbt.3437
31. Chari R, Mali P, Moosburner M *et al.* Unraveling CRISPR-Cas9 genome engineering parameters via a library-on-library approach. *Nat Methods* 2015;**12**:823–6. https://doi.org/10.1038/nmeth.3473
32. Wang T, Wei JJ, Sabatini DM *et al.* Genetic screens in human cells using the CRISPR-Cas9 system. *Science* 2014;**343**:80–4. https://doi.org/10.1126/science.1246981
33. Stemmer M, Thumberger T, Del Sol Keyer M *et al.* CCTop: an intuitive, flexible and reliable CRISPR/Cas9 target prediction tool. *PLoS One* 2015;**10**:e0124633. https://doi.org/10.1371/journal.pone.0124633
34. Brinkman EK, Chen T, Amendola M *et al.* Easy quantitative assessment of genome editing by sequence trace decomposition. *Nucleic Acids Res* 2014;**42**:e168. https://doi.org/10.1093/nar/gku936
35. Clement K, Rees H, Canver MC *et al.* CRISPResso2 provides accurate and rapid genome editing sequence analysis. *Nat Biotechnol* 2019;**37**:224–6. https://doi.org/10.1038/s41587-019-0032-3
36. Varshney GK, Carrington B, Pei W *et al.* A high-throughput functional genomics workflow based on CRISPR/Cas9-mediated targeted mutagenesis in zebrafish. *Nat Protoc* 2016;**11**:2357–75. https://doi.org/10.1038/nprot.2016.141
37. Patterson AS, Dugdale J, Koleilat A *et al.* Vital dye uptake of YO-PRO-1 and DASPEI depends upon mechanoelectrical transduction function in zebrafish hair cells. *JARO* 2024;**25**:531–43. https://doi.org/10.1007/s10162-024-00967-w
38. Petree C, Varshney GK. MultiFRAGing: rapid and simultaneous genotyping of multiple alleles in a single reaction. *Sci Rep* 2020;**10**:531–43. https://doi.org/10.1038/s41598-020-59986-1
39. Lin SJ, Vona B, Porter HM *et al.* Biallelic variants in WARS1 cause a highly variable neurodevelopmental syndrome and implicate a critical exon for normal auditory function. *Hum Mutat* 2022;**43**:1472–89. https://doi.org/10.1002/humu.24435
40. Cali E, Lin SJ, Rocca C *et al.* A homozygous MED11 C-terminal variant causes a lethal neurodegenerative disease. *Genet Med* 2022;**24**:2194–203. https://doi.org/10.1016/j.gim.2022.07.013
41. Thisse B, Thisse C. In situ hybridization on whole-mount zebrafish embryos and young larvae. *Methods Mol Biol* 2014;**1211**:53–67. https://doi.org/10.1007/978-1-4939-1459-3_5
42. Lin SJ, Vona B, Barbalho PG *et al.* Biallelic variants in KARS1 are associated with neurodevelopmental disorders and hearing loss recapitulated by the knockout zebrafish. *Genet Med* 2021;**23**:1933–43. https://doi.org/10.1038/s41436-021-01239-1
43. Kaiyrzhanov R, Rad A, Lin SJ *et al.* Bi-allelic ACBD6 variants lead to a neurodevelopmental syndrome with progressive and complex movement disorders. *Brain* 2024;**147**:1436–56. https://doi.org/10.1093/brain/awad380
44. Richard EM, Bakhtiari S, Marsh APL *et al.* Bi-allelic variants in SPATA5L1 lead to intellectual disability, spastic-dystonic cerebral palsy, epilepsy, and hearing loss. *Am Hum Genet* 2021;**108**:2006–16. https://doi.org/10.1016/j.ajhg.2021.08.003
45. Erickson T, Morgan CP, Olt J *et al.* Integration of Tmc1/2 into the mechanotransduction complex in zebrafish hair cells is regulated by transmembrane O-methyltransferase (Tomt). *eLife* 2017;**6**:e28474. https://doi.org/10.7554/eLife.28474
46. Kim SH, Wu SY, Baek JI *et al.* A post-developmental genetic screen for zebrafish models of inherited liver disease. *PLoS One* 2015;**10**:e0125980. https://doi.org/10.1371/journal.pone.0125980
47. Walker MB, Kimmel CB. A two-color acid-free cartilage and bone stain for zebrafish larvae. *Biotech Histochem* 2007;**82**:23–8. https://doi.org/10.1080/10520290701333558
48. Halpern ME, Thisse C, Ho RK *et al.* Cell-autonomous shift from axial to paraxial mesodermal development in zebrafish floating head mutants. *Development* 1995;**121**:4257–64. https://doi.org/10.1242/dev.121.12.4257
49. Kelsh RN, Brand M, Jiang YJ *et al.* Zebrafish pigmentation mutations and the processes of neural crest development. *Development* 1996;**123**:369–89. https://doi.org/10.1242/dev.123.1.369
50. Loosli F, Staub W, Finger-Baier KC *et al.* Loss of eyes in zebrafish caused by mutation of chokh/rx3. *EMBO Rep* 2003;**4**:894–9. https://doi.org/10.1038/sj.embor.embor919
51. Akanuma T, Koshida S, Kawamura A *et al.* Paf1 complex homologues are required for Notch-regulated transcription during somite segmentation. *EMBO Rep* 2007;**8**:858–63. https://doi.org/10.1038/sj.embor.7401045
52. Shi J, Wang E, Milazzo JP *et al.* Discovery of cancer drug targets by CRISPR-Cas9 screening of protein domains. *Nat Biotechnol* 2015;**33**:661–7. https://doi.org/10.1038/nbt.3235
53. Munoz DM, Cassiani PJ, Li L *et al.* CRISPR screens provide a comprehensive assessment of cancer vulnerabilities but generate false-positive hits for highly amplified genomic regions. *Cancer Discov* 2016;**6**:900–13. https://doi.org/10.1158/2159-8290.CD-16-0178
54. He W, Zhang L, Villarreal OD *et al.* De novo identification of essential protein domains from CRISPR-Cas9 tiling-sgRNA

knockout screens. *Nat Commun* 2019;**10**:4541. https://doi.org/10.1038/s41467-019-12489-8
55. Wang WD, Melville DB, Montero-Balaguer M *et al.* Tfap2a and Foxd3 regulate early steps in the development of the neural crest progenitor population. *Dev Biol* 2011;**360**:173–85. https://doi.org/10.1016/j.ydbio.2011.09.019
56. Lvovs D, Favorova OO, Favorov AV. A polygenic approach to the study of polygenic diseases. *Acta Naturae* 2012;**4**:59–71.
57. Haddad FS, Manne RK. Involvement of the penis by rectocolic adenocarcinoma. Report of a case and review of the literature. *Dis Colon Rectum* 1987;**30**:123–9. https://doi.org/10.1007/BF02554950
58. El-Brolosy MA, Kontarakis Z, Rossi A *et al.* Genetic compensation triggered by mutant mRNA degradation. *Nature* 2019;**568**:193–7. https://doi.org/10.1038/s41586-019-1064-z
59. Ma Z, Zhu P, Shi H *et al.* PTC-bearing mRNA elicits a genetic compensation response via Upf3a and COMPASS components. *Nature* 2019;**568**:259–63. https://doi.org/10.1038/s41586-019-1057-y
60. Leerberg DM, Hopton RE, Draper BW. Fibroblast growth factor receptors function redundantly during zebrafish embryonic development. *Genetics* 2019;**212**:1301–19. https://doi.org/10.1534/genetics.119.302345
61. Guarente L. Synthetic enhancement in gene interaction: a genetic tool come of age. *Trends Genet* 1993;**9**:362–6. https://doi.org/10.1016/0168-9525(93)90042-G
62. Reischauer S, Levesque MP, Nusslein-Volhard C *et al.* Lgl2 executes its function as a tumor suppressor by regulating ErbB signaling in the zebrafish epidermis. *PLoS Genet* 2009;**5**:e1000720. https://doi.org/10.1371/journal.pgen.1000720
63. Bogershausen N, Krawczyk HE, Jamra RA *et al.* WARS1 and SARS1: two tRNA synthetases implicated in autosomal recessive microcephaly. *Hum Mutat* 2022;**43**:1454–71. https://doi.org/10.1002/humu.24430
64. Cardoso AR, Lopes-Marques M, Silva RM *et al.* Essential genetic findings in neurodevelopmental disorders. *Hum Genomics* 2019;**13**:31. https://doi.org/10.1186/s40246-019-0216-4
65. Moreno-De-Luca A, Myers SM, Challman TD *et al.* Developmental brain dysfunction: revival and expansion of old concepts based on new genetic evidence. *The Lancet Neurology* 2013;**12**:406–14. https://doi.org/10.1016/S1474-4422(13)70011-5
66. Dougnon G, Matsui H. Modelling autism spectrum disorder (ASD) and attention-deficit/hyperactivity disorder (ADHD) using mice and Zebrafish. *Int J Mol Sci* 2022;**23**:7550. https://doi.org/10.3390/ijms23147550
67. Rosa JGS, Lima C, Lopes-Ferreira M. Zebrafish larvae behavior models as a tool for drug screenings and pre-clinical trials: a review. *Int J Mol Sci* 2022;**23**:6647. https://doi.org/10.3390/ijms23126647
68. Tonon F, Grassi G. Zebrafish as an experimental model for Human disease. *Int J Mol Sci* 2023;**24**:8771. https://doi.org/10.3390/ijms24108771
69. Bradford YM, Van Slyke CE, Ruzicka L *et al.* Zebrafish information network, the knowledgebase for Danio rerio research. *Genetics* 2022;**220**:iyac016. https://doi.org/10.1093/genetics/iyac016
70. Chen L, Li Y, Sottas C *et al.* Loss of mitochondrial ATPase ATAD3A contributes to nonalcoholic fatty liver disease through accumulation of lipids and damaged mitochondria. *J Biol Chem* 2022;**298**:102008. https://doi.org/10.1016/j.jbc.2022.102008
71. Peeters-Scholte C, Adama van Scheltema PN, Klumper F *et al.* Genotype-phenotype correlation in ATAD3A deletions: not just of scientific relevance. *Brain* 2017;**140**:e66. https://doi.org/10.1093/brain/awx239
72. Cooper HM, Yang Y, Ylikallio E *et al.* ATPase-deficient mitochondrial inner membrane protein ATAD3A disturbs mitochondrial dynamics in dominant hereditary spastic paraplegia. *Hum Mol Genet* 2017;**26**:1432–43. https://doi.org/10.1093/hmg/ddx042
73. Desai R, Frazier AE, Durigon R *et al.* ATAD3 gene cluster deletions cause cerebellar dysfunction associated with altered mitochondrial DNA and cholesterol metabolism. *Brain* 2017;**140**:1595–610. https://doi.org/10.1093/brain/awx094
74. Pillai NR, AlDhaheri NS, Ghosh R *et al.* Biallelic variants in COX4I1 associated with a novel phenotype resembling Leigh syndrome with developmental regression, intellectual disability, and seizures. *American J of Med Genetics Pt A* 2019;**179**:2138–43. https://doi.org/10.1002/ajmg.a.61288
75. Torres-Hernandez BA, Colon LR, Rosa-Falero C *et al.* Reversal of pentylenetetrazole-altered swimming and neural activity-regulated gene expression in zebrafish larvae by valproic acid and valerian extract. *Psychopharmacology (Berl)* 2016;**233**:2533–47. https://doi.org/10.1007/s00213-016-4304-z
76. Shearer AE, Hildebrand MS, Odell AM *et al.* Genetic Hearing Loss Overview. In: Adam MP, Feldman J, Mirzaa GM *et al.* . (eds.), *GeneReviews [Internet]*. Seattle (WA): University of Washington, 2023. https://www.ncbi.nlm.nih.gov/books/NBK1434/
77. Whitfield TT. Zebrafish as a model for hearing and deafness. *J Neurobiol* 2002;**53**:157–71. https://doi.org/10.1002/neu.10123
78. Blanco-Sanchez B, Clement A, Phillips JB *et al.* Zebrafish models of human eye and inner ear diseases. *Methods Cell Biol* 2017;**138**:415–67. https://doi.org/10.1016/bs.mcb.2016.10.006
79. Vona B, Doll J, Hofrichter MAH *et al.* Small fish, big prospects: using zebrafish to unravel the mechanisms of hereditary hearing loss. *Hear Res* 2020;**397**:107906. https://doi.org/10.1016/j.heares.2020.107906
80. Sheets L, Holmgren M, Kindt KS. How zebrafish can drive the future of genetic-based hearing and balance research. *JARO* 2021;**22**:215–35. https://doi.org/10.1007/s10162-021-00798-z
81. Lundberg YW, Xu Y, Thiessen KD *et al.* Mechanisms of otoconia and otolith development. *Dev Dyn* 2015;**244**:239–53. https://doi.org/10.1002/dvdy.24195
82. Yao Q, Wang L, Mittal R *et al.* Transcriptomic analyses of inner ear sensory epithelia in zebrafish. *Anat Rec* 2020;**303**:527–43. https://doi.org/10.1002/ar.24331
83. Baeza-Loya S, Raible DW. Vestibular physiology and function in zebrafish. *Front Cell Dev Biol* 2023;**11**:1172933. https://doi.org/10.3389/fcell.2023.1172933
84. Lush ME, Diaz DC, Koenecke N *et al.* scRNA-seq reveals distinct stem cell populations that drive hair cell regeneration after loss of Fgf and Notch signaling. *eLife* 2019;**8**:e44431. https://doi.org/10.7554/eLife.44431
85. Baek S, Tran NTT, Diaz DC *et al.* Single-cell transcriptome analysis reveals three sequential phases of gene expression during zebrafish sensory hair cell regeneration. *Dev Cell* 2022;**57**:799–819. https://doi.org/10.1016/j.devcel.2022.03.001
86. Shi T, Beaulieu MO, Saunders LM *et al.* Single-cell transcriptomic profiling of the zebrafish inner ear reveals molecularly distinct hair cell and supporting cell subtypes. *eLife* 2023;**12**:e82978. https://doi.org/10.7554/eLife.82978
87. Malicki J, Schier AF, Solnica-Krezel L *et al.* Mutations affecting development of the zebrafish ear. *Development* 1996;**123**:275–83. https://doi.org/10.1242/dev.123.1.275
88. Stooke-Vaughan GA, Obholzer ND, Baxendale S *et al.* Otolith tethering in the zebrafish otic vesicle requires Otogelin and alpha-tectorin. *Development* 2015;**142**:1137–45. https://doi.org/10.1242/dev.116632
89. Tohme M, Prud'homme SM, Boulahtouf A *et al.* Estrogen-related receptor gamma is an in vivo receptor of bisphenol A. *FASEB J* 2014;**28**:3124–33. https://doi.org/10.1096/fj.13-240465
90. Murayama E, Herbomel P, Kawakami A *et al.* Otolith matrix proteins OMP-1 and Otolin-1 are necessary for normal otolith growth and their correct anchoring onto the sensory maculae. *Mech Dev* 2005;**122**:791–803. https://doi.org/10.1016/j.mod.2005.03.002

91. Jin D, Ni TT, Sun J *et al.* Prostaglandin signalling regulates ciliogenesis by modulating intraflagellar transport. *Nat Cell Biol* 2014;**16**:841–51. https://doi.org/10.1038/ncb3029
92. Sollner C, Burghammer M, Busch-Nentwich E *et al.* Control of crystal size and lattice formation by starmaker in otolith biomineralization. *Science* 2003;**302**:282–6. https://doi.org/10.1126/science.1088443
93. Kang YJ, Stevenson AK, Yau PM *et al.* Sparc protein is required for normal growth of zebrafish otoliths. *JARO* 2008;**9**:436–51. https://doi.org/10.1007/s10162-008-0137-8
94. Yang CH, Cheng CH, Chen GD *et al.* Zona pellucida domain-containing protein beta-tectorin is crucial for zebrafish proper inner ear development. *PLoS One* 2011;**6**:e23078. https://doi.org/10.1371/journal.pone.0023078
95. Solomon KS, Fritz A. Concerted action of two dlx paralogs in sensory placode formation. *Development* 2002;**129**:3127–36. https://doi.org/10.1242/dev.129.13.3127
96. Yariz KO, Duman D, Zazo Seco C *et al.* Mutations in OTOGL, encoding the inner ear protein otogelin-like, cause moderate sensorineural hearing loss. *Am Hum Genet* 2012;**91**:872–82. https://doi.org/10.1016/j.ajhg.2012.09.011
97. Erickson T, Nicolson T. Identification of sensory hair-cell transcripts by thiouracil-tagging in zebrafish. *BMC Genomics* 2015;**16**:842. https://doi.org/10.1186/s12864-015-2072-5
98. Asamura K, Abe S, Imamura Y *et al.* Type IX collagen is crucial for normal hearing. *Neuroscience* 2005;**132**:493–500. https://doi.org/10.1016/j.neuroscience.2005.01.013
99. Avan P, Le Gal S, Michel V *et al.* Otogelin, otogelin-like, and stereocilin form links connecting outer hair cell stereocilia to each other and the tectorial membrane. *Proc Natl Acad Sci USA* 2019;**116**:25948–57. https://doi.org/10.1073/pnas.1902781116
100. Nicolson T. The genetics of hair-cell function in zebrafish. *J Neurogenet* 2017;**31**:102–12. https://doi.org/10.1080/01677063.2017.1342246
101. Kwak SJ, Vemaraju S, Moorman SJ *et al.* Zebrafish pax5 regulates development of the utricular macula and vestibular function. *Dev Dyn* 2006;**235**:3026–38. https://doi.org/10.1002/dvdy.20961
102. Carlson RJ, Avraham KB. Emerging complexities of the mouse as a model for human hearing loss. *Proc Natl Acad Sci USA* 2022;**119**:e2211351119. https://doi.org/10.1073/pnas.2211351119
103. Horn HF, Brownstein Z, Lenz DR *et al.* The LINC complex is essential for hearing. *J Clin Invest* 2013;**123**:740–50.
104. Tona R, Chen W, Nakano Y *et al.* The phenotypic landscape of a Tbc1d24 mutant mouse includes convulsive seizures resembling human early infantile epileptic encephalopathy. *Hum Mol Genet* 2019;**28**:1530–47. https://doi.org/10.1093/hmg/ddy445
105. Tona R, Lopez IA, Fenollar-Ferrer C *et al.* Mouse models of Human pathogenic variants of TBC1D24 associated with non-syndromic deafness DFNB86 and DFNA65 and syndromes involving deafness. *Genes* 2020;**11**:1122. https://doi.org/10.3390/genes11101122
106. Kok FO, Shin M, Ni CW *et al.* Reverse genetic screening reveals poor correlation between morpholino-induced and mutant phenotypes in zebrafish. *Dev Cell* 2015;**32**:97–108. https://doi.org/10.1016/j.devcel.2014.11.018
107. Xie A, Ma Z, Wang J *et al.* Upf3a but not Upf1 mediates the genetic compensation response induced by leg1 deleterious mutations in an H3K4me3-independent manner. *Cell Discov* 2023;**9**:63. https://doi.org/10.1038/s41421-023-00550-2
108. Lin SJ, Vona B, Lau T *et al.* Evaluating the association of biallelic OGDHL variants with significant phenotypic heterogeneity. *Genome Med* 2023;**15**:102. https://doi.org/10.1186/s13073-023-01258-4
109. Buglo E, Sarmiento E, Martuscelli NB *et al.* Genetic compensation in a stable slc25a46 mutant zebrafish: a case for using F0 CRISPR mutagenesis to study phenotypes caused by inherited disease. *PLoS One* 2020;**15**:e0230566. https://doi.org/10.1371/journal.pone.0230566
110. She J, Wu Y, Lou B *et al.* Genetic compensation by epob in pronephros development in epoa mutant zebrafish. *Cell Cycle* 2019;**18**:2683–96. https://doi.org/10.1080/15384101.2019.1656019
111. Kwon TJ, Cho HJ, Kim UK *et al.* Methionine sulfoxide reductase B3 deficiency causes hearing loss due to stereocilia degeneration and apoptotic cell death in cochlear hair cells. *Hum Mol Genet* 2014;**23**:1591–601. https://doi.org/10.1093/hmg/ddt549
112. Ali RA, Rehman AU, Khan SN *et al.* DFNB86, a novel autosomal recessive non-syndromic deafness locus on chromosome 16p13.3. *Clin Genet* 2012;**81**:498–500. https://doi.org/10.1111/j.1399-0004.2011.01729.x
113. Charizopoulou N, Lelli A, Schraders M *et al.* Gipc3 mutations associated with audiogenic seizures and sensorineural hearing loss in mouse and human. *Nat Commun* 2011;**2**:201. https://doi.org/10.1038/ncomms1200
114. JanssensdeVarebeke SPF, Van Camp G, Peeters N *et al.* Bi-allelic inactivating variants in the COCH gene cause autosomal recessive prelingual hearing impairment. *Eur J Hum Genet* 2018;**26**:587–91. https://doi.org/10.1038/s41431-017-0066-2
115. Vahava O, Morell R, Lynch ED *et al.* Mutation in transcription factor POU4F3 associated with inherited progressive hearing loss in humans. *Science* 1998;**279**:1950–4. https://doi.org/10.1126/science.279.5358.1950
116. Wallmeroth D, Lackmann JW, Kueckelmann S *et al.* Human UPF3A and UPF3B enable fault-tolerant activation of nonsense-mediated mRNA decay. *EMBO J* 2022;**41**:e109191. https://doi.org/10.15252/embj.2021109191
117. Ding Y, Wang M, Bu H *et al.* Application of an F0-based genetic assay in adult zebrafish to identify modifier genes of an inherited cardiomyopathy. *Dis Model Mech* 2023;**16**:dmm049427. https://doi.org/10.1242/dmm.049427
118. Klatt Shaw D, Mokalled MH. Efficient CRISPR/Cas9 mutagenesis for neurobehavioral screening in adult zebrafish. *G3* 2021;**11**:jkab089. https://doi.org/10.1093/g3journal/jkab089
119. Lu F, Leach LL, Gross JM. A CRISPR-Cas9-mediated F0 screen to identify pro-regenerative genes in the zebrafish retinal pigment epithelium. *Sci Rep* 2023;**13**:3142. https://doi.org/10.1038/s41598-023-29046-5
120. Moreno-Campos R, Singleton EW, Uribe RA. A targeted CRISPR-Cas9 mediated F0 screen identifies genes involved in establishment of the enteric nervous system. *PLoS One* 2024;**19**:e0303914. https://doi.org/10.1371/journal.pone.0303914
121. Quick RE, Buck LD, Parab S *et al.* Highly efficient synthetic CRISPR RNA/Cas9-based mutagenesis for rapid cardiovascular phenotypic screening in F0 zebrafish. *Front. Cell Dev. Biol.* 2021;**9**:735598. https://doi.org/10.3389/fcell.2021.735598
122. Hwang WY, Fu Y, Reyon D *et al.* Heritable and precise zebrafish genome editing using a CRISPR-Cas system. *PLoS One* 2013;**8**:e68708. https://doi.org/10.1371/journal.pone.0068708
123. Wetzel AS, Darbro BW. A comprehensive list of human microdeletion and microduplication syndromes. *BMC Genom Data* 2022;**23**:82. https://doi.org/10.1186/s12863-022-01093-3
124. Colon-Rodriguez A, Uribe-Salazar JM, Weyenberg KB *et al.* Assessment of autism zebrafish mutant models using a high-throughput larval phenotyping platform. *Front Cell Dev Biol* 2020;**8**:586296. https://doi.org/10.3389/fcell.2020.586296
125. Parvez S, Herdman C, Beerens M *et al.* MIC-Drop: a platform for large-scale in vivo CRISPR screens. *Science* 2021;**373**:1146–51. https://doi.org/10.1126/science.abi8870

Received: June 7, 2024. **Revised:** February 14, 2025. **Editorial Decision:** February 17, 2025. **Accepted:** February 24, 2025